Atmos. Chem. Phys., 18, 735–756, 2018
https://doi.org/10.5194/acp-18-735-2018


Atmospheric Chemistry and Physics
Open Access
EGU

# Top-down constraints on global $N_2O$ emissions at optimal resolution: application of a new dimension reduction technique

**Kelley C. Wells[1], Dylan B. Millet[1], Nicolas Bousserez[2], Daven K. Henze[2], Timothy J. Griffis[1], Sreelekha Chaliyakunnel[1], Edward J. Dlugokencky[3], Eri Saikawa[4], Gao Xiang[5], Ronald G. Prinn[6], Simon O'Doherty[7], Dickon Young[7], Ray F. Weiss[8], Geoff S. Dutton[3,9], James W. Elkins[3], Paul B. Krummel[10], Ray Langenfelds[10], and L. Paul Steele[10]**

[1]Department of Soil, Water, and Climate, University of Minnesota, St. Paul, MN, USA
[2]Department of Mechanical Engineering, University of Colorado at Boulder, Boulder, CO, USA
[3]Earth System Research Laboratory, NOAA, Boulder, CO, USA
[4]Department of Environmental Sciences, Emory University, Atlanta, GA, USA
[5]Joint Program on the Science and Policy of Global Change, Massachusetts Institute of Technology, Cambridge, MA, USA
[6]Center for Global Change Science, Massachusetts Institute of Technology, Cambridge, MA, USA
[7]School of Chemistry, University of Bristol, Bristol, UK
[8]Scripps Institute of Oceanography, University of California San Diego, La Jolla, CA, USA
[9]CIRES, University of Colorado at Boulder, Boulder, CO, USA
[10]Climate Science Centre, CSIRO Oceans and Atmosphere, Aspendale, Victoria, Australia

**Correspondence:** Dylan B. Millet (dbm@umn.edu)

Received: 6 July 2017 – Discussion started: 14 August 2017
Revised: 17 November 2017 – Accepted: 10 December 2017 – Published: 22 January 2018

**Abstract.** We present top-down constraints on global monthly $N_2O$ emissions for 2011 from a multi-inversion approach and an ensemble of surface observations. The inversions employ the GEOS-Chem adjoint and an array of aggregation strategies to test how well current observations can constrain the spatial distribution of global $N_2O$ emissions. The strategies include (1) a standard 4D-Var inversion at native model resolution ($4° \times 5°$), (2) an inversion for six continental and three ocean regions, and (3) a fast 4D-Var inversion based on a novel dimension reduction technique employing randomized singular value decomposition (SVD). The optimized global flux ranges from 15.9 Tg N $yr^{-1}$ (SVD-based inversion) to 17.5–17.7 Tg N $yr^{-1}$ (continental-scale, standard 4D-Var inversions), with the former better capturing the extratropical $N_2O$ background measured during the HIAPER Pole-to-Pole Observations (HIPPO) airborne campaigns. We find that the tropics provide a greater contribution to the global $N_2O$ flux than is predicted by the prior bottom-up inventories, likely due to underestimated agricultural and oceanic emissions. We infer an overestimate of natural soil emissions in the extratropics and find that predicted emissions are seasonally biased in northern midlatitudes. Here, optimized fluxes exhibit a springtime peak consistent with the timing of spring fertilizer and manure application, soil thawing, and elevated soil moisture. Finally, the inversions reveal a major emission underestimate in the US Corn Belt in the bottom-up inventory used here. We extensively test the impact of initial conditions on the analysis and recommend formally optimizing the initial $N_2O$ distribution to avoid biasing the inferred fluxes. We find that the SVD-based approach provides a powerful framework for deriving emission information from $N_2O$ observations: by defining the optimal resolution of the solution based on the information content of the inversion, it provides spatial information that is lost when aggregating to political or geographic regions, while also providing more temporal information than a standard 4D-Var inversion.

## 1 Introduction

Nitrous oxide ($N_2O$) is a long-lived greenhouse gas ($\tau \sim$ 122–131 years; Volk et al., 1997; Prather et al., 2012) with substantial impacts on both climate and stratospheric chem-

istry. It has a global warming potential far exceeding that of $CO_2$ (265× on a 100-year timescale; Myhre et al., 2013), and its emissions weighted by ozone depletion potential currently exceed those of all other substances (Ravishankara et al., 2009). The global $N_2O$ source is reasonably well constrained (15.7 to 20.1 $Tg\,N\,yr^{-1}$ for years 1999–2009; Prather et al., 2012; Saikawa et al., 2014; Thompson et al., 2014a, c) by its atmospheric abundance and estimated lifetime. However, attribution of this source to specific regions and sectors has been hindered by the sparse global observing network and by the weak variability in $N_2O$ mixing ratios (e.g., Wells et al., 2015). Quantitative interpretation of atmospheric $N_2O$ measurements in terms of globally resolved emissions thus first requires a rigorous assessment of how results hinge on the modeling framework employed. Here, we apply a hierarchy of model resolutions, including a new method that formally defines the state vector for optimization based on the information content of the observations, in a global inverse modeling framework to address this need. We use this model hierarchy with a global suite of observations to (i) quantify the spatial and seasonal distribution of $N_2O$ emissions for 2011, (ii) examine what features of these results are robust across model configurations, and (iii) assess the implications for current understanding of the $N_2O$ budget and future research needs.

The primary sources of atmospheric $N_2O$ are microbial denitrification and nitrification, which lead to $N_2O$ production in soils (Firestone and Davidson, 1989), ocean waters (Elkins et al., 1978; Cohen and Gordon, 1979), and in streams, rivers, and lakes (Seitzinger and Kroeze, 1998; Beaulieu et al., 2011). Global mean $N_2O$ mixing ratios rose by $0.85 \pm 0.1\,ppb\,yr^{-1}$ from 2001 to 2015 (based on NOAA surface measurements) primarily due to increased use of inorganic fertilizers and manure (Galloway et al., 2008; Davidson, 2009; Park et al., 2012) and the nonlinear response of $N_2O$ emissions to N inputs in some agricultural systems (Shcherbak et al., 2014). Estimates for the global agricultural flux range from 4.3 to 6.3 $Tg\,N\,yr^{-1}$ (Mosier et al., 1998; Crutzen et al., 2008; Davidson, 2009): this includes emissions occurring on-field (i.e., "direct" emissions from fertilized fields), downstream ("indirect" emissions from N leaching and runoff, and from deposition of volatilized $NO_x$ and $NH_3$), and from manure management. These sources are all subject to large uncertainties. For example, by assuming a linear flux response to fertilizer application, one can either under- or overestimate emissions depending on the application rate (Shcherbak et al., 2014; Gerber et al., 2016). Recent work also suggests that the indirect $N_2O$ flux could be 2.6–9 times larger than is presently accounted for in bottom-up estimates (Griffis et al., 2013; Turner et al., 2015b), which would imply an underestimate of the agricultural contribution to the overall $N_2O$ budget. Nonagricultural soils and oceans are thought to contribute an additional 7.4–11 $Tg\,N\,yr^{-1}$ (Saikawa et al., 2013) and 1.2–6.8 $Tg\,N\,yr^{-1}$ (Nevison et al., 1995; Jin and Gruber, 2003; Manizza et al., 2012), respectively, to the global $N_2O$ source. Industrial, transportation, and biomass burning emissions also exist but are thought to be relatively minor, totaling 1.2–1.8 $Tg\,N\,yr^{-1}$ (Prather et al., 2001).

Because microbial nitrification and denitrification, and the subsequent soil–atmosphere $N_2O$ flux, depend strongly on factors such as soil moisture, temperature, physical characteristics, and N availability (e.g., Potter et al., 1996; Bouwman, 1998; Kim et al., 2012; Bouwman et al., 2013; Butterbach-Bahl et al., 2013; Griffis et al., 2017), $N_2O$ emissions can exhibit major temporal and spatial variability. For example, Wagner-Riddle et al. (2017) found that short-duration freeze–thaw cycles can account for 35–65 % of the annual direct $N_2O$ emissions from seasonally frozen croplands and that neglecting this contribution would lead to a 17–28 % underestimate of the global $N_2O$ source (direct + indirect) from agricultural soils. This type of variability poses a major challenge to bottom-up and top-down efforts to quantify $N_2O$ surface fluxes and attribute them to specific times, locations, and mechanisms. The relatively sparse coverage of measurement sites and low atmospheric variability (because of the long $N_2O$ lifetime, surface mixing ratios typically vary by $< 10$ ppb on a $\sim 325$ ppb background) compound the challenge and limit the spatial and temporal resolution at which emission fluxes can be inferred (Wells et al., 2015). As a result, global $N_2O$ inversions often employ some aggregation strategy to optimize emissions for a small set of geographic regions (e.g., Hirsch et al., 2006; Huang et al., 2008; Saikawa et al., 2014). However, in the past this aggregation has been done based on physical or political boundaries rather than by formally determining the degrees of freedom (DOFs) in the inverse system – which leads to aggregation errors and sub-optimal results. Work on $CO_2$ inversions has also highlighted this issue (e.g., Kaminski et al., 2001) and the resulting importance of determining the proper state vector size for optimal results (Bocquet et al., 2011).

Another key challenge is that because of the long $N_2O$ lifetime, inaccuracies in model initial conditions can lead to large biases in the subsequent optimized emissions (Thompson et al., 2014c). Past global $N_2O$ inversion studies have established the initial conditions in a variety of ways: from a forward model spinup that is then evaluated against observations (e.g., Huang et al., 2008); by including the initial condition as a separate adjustable parameter in the source optimization (e.g., Saikawa et al., 2014; Thompson et al., 2014a); or from interpolation of atmospheric observations (e.g., Wells et al., 2015). To our knowledge there has not yet been a detailed evaluation of these different methods and their impacts on $N_2O$ source inversions. Such information is needed to establish the degree to which uncertainties in the initial conditions can propagate to errors in the optimized $N_2O$ emission estimates.

In this paper, we address the above uncertainties in a quantitative way using a multi-inversion hierarchy to derive top-down constraints on $N_2O$ emissions for 2011. We use the ad-

joint of the GEOS-Chem chemical transport model (CTM) to solve for monthly fluxes at the model grid box scale as well as at geographically aggregated continental scales. We compare these results with those obtained using a new dimension reduction technique based on the singular value decomposition (SVD) of the so-called prior-preconditioned Hessian of the 4D-Var cost function (Bousserez and Henze, 2017). This new SVD-based approach allows us to solve for fluxes at optimal spatiotemporal resolution, as defined by the information content of the $N_2O$ observations – thus maximizing the DOFs for the inversion and avoiding any need for spatial aggregation based on geography or source type. It also offers significant time savings over standard grid-based 4D-Var approaches due to the use of efficient randomized-SVD algorithms (Halko et al., 2011). The initial conditions for the above inversions are constructed in a variety of ways, and we use observations and model simulations to assess their accuracy and associated impacts on optimized $N_2O$ fluxes. We then evaluate these optimized emissions using independent airborne measurements and interpret the results in terms of underlying emission processes, with specific emphasis on the role of model resolution in affecting the solution and on those features that appear most robust (and most uncertain) across model configurations.

## 2 Methods

### 2.1 GEOS-Chem $N_2O$ simulation

The $N_2O$ simulation employed here, previously described by Wells et al. (2015), is based on the GEOS-Chem CTM (www.geos-chem.org) with GEOS-5 assimilated meteorological data from the NASA Goddard Earth Observing System. We use a horizontal resolution of $4° \times 5°$ with 47 vertical levels from the surface to 0.01 hPa as well as time steps of 30 min for transport and 60 min for emissions and chemistry. The simulation period spans April 2010–April 2012 (the start date is selected to match the initiation of $N_2O$ measurements at the KCMP tall tower site discussed later).

A priori $N_2O$ emissions for anthropogenic, nonagricultural sources (including industrial processes, transportation, residential, and wastewater emissions) are from the Emission Database for Global Atmospheric Research (EDGARv4.2; http://edgar.jrc.ec.europa.eu), which are provided annually and total $1.7\,\mathrm{Tg\,N\,yr^{-1}}$ for 2008. Monthly $N_2O$ emissions from nonagricultural soils are from CLMCN-$N_2O$ as described by Saikawa et al. (2013) and total $7.5\,\mathrm{Tg\,N\,yr^{-1}}$ for 2011. These emissions have been shown to accurately capture the magnitude and seasonality of soil emissions in the Amazon, but exhibited less skill in reproducing the observed seasonal cycle in northern midlatitudes (based on data from New Hampshire; Saikawa et al., 2013). The magnitude of these emissions varies depending on the meteorological forcing dataset used; forcings used here are from the MIT Integrated Global System Model (IGSM) fully coupled transient 20th century climate integration (Sokolov et al., 2009). Adding these to the annual EDGARv4.2 direct and indirect (leaching and runoff) agricultural emissions ($3.5\,\mathrm{Tg\,N\,yr^{-1}}$), indirect emissions from $NO_x$ and $NH_3$ deposition ($0.4\,\mathrm{Tg\,N\,yr^{-1}}$), and emissions from manure management ($0.2\,\mathrm{Tg\,N\,yr^{-1}}$) leads to an a priori global soil $N_2O$ source of $11.6\,\mathrm{Tg\,N\,yr^{-1}}$ for 2011. Biomass burning emissions are computed monthly based on the Global Fire Emissions Database version 3 (GFED3; van der Werf et al., 2010), totaling $0.6\,\mathrm{Tg\,N\,yr^{-1}}$, while monthly oceanic $N_2O$ emissions are from Jin and Gruber (2003) and total $3.5\,\mathrm{Tg\,N\,yr^{-1}}$. The global annual a priori $N_2O$ flux for 2011 is then $17.4\,\mathrm{Tg\,N\,yr^{-1}}$, in the range of recent top-down estimates ($16.1$–$18.7\,\mathrm{Tg\,N\,yr^{-1}}$ for years 2006–2008; Saikawa et al., 2014; Thompson et al., 2014c). Stratospheric loss of $N_2O$ via photolysis and reaction with $O(^1D)$ is calculated from 3-D loss frequencies archived monthly from Global Modeling Initiative (GMI) simulations driven by MERRA meteorological fields; the resulting $N_2O$ lifetime is $\sim$ 127 years (note that the value depends on the initial spatial distribution of $N_2O$ in the model).

The long $N_2O$ lifetime necessitates accurate characterization of initial conditions to avoid biasing the optimized fluxes (e.g., Thompson et al., 2014c). In our work, we construct six sets of initial conditions from global $N_2O$ observations and evaluate the corresponding impacts on the inferred fluxes. Initial condition fields are constructed based on either data interpolation or 4D-Var optimization, with details discussed in Sect. 3.

### 2.2 Inversion frameworks

We employ three inversion methods with varying resolution to solve for monthly $N_2O$ emissions over 2 years (April 2010–April 2012) based on global surface observations. The first of these is a 4D-Var inversion that iteratively optimizes emissions on the native model grid (here $4° \times 5°$) using gradients computed with the GEOS-Chem adjoint model. This has the advantage of avoiding any aggregation errors associated with traditional clustering methods. However, our previous work (Wells et al., 2015) has shown that the degrees of freedom for atmospheric $N_2O$ inversions is typically much less than the native model grid dimension and, furthermore, that native resolution optimizations have limited ability to resolve any temporal (e.g., seasonal) $N_2O$ emission biases. We therefore apply two alternate approaches to reduce the dimension of the inverse problem: (1) a 4D-Var inversion solving for emissions on aggregated, geographically defined land and ocean regions and (2) a 4D-Var inversion solving for emissions on a reduced emission basis set defined using an SVD-based information content analysis. In all three frameworks we consider two emission sectors (terrestrial and oceanic) and optimize monthly fluxes.

We present details for each of the three frameworks in the following sections.

#### 2.2.1 Standard 4D-Var inversion

Our standard inversion is a 4D-Var optimization in which the state vector contains scaling factors for monthly $N_2O$ emissions at $4° \times 5°$. The optimal set of emission scaling factors is obtained by minimizing the cost function, $J(\boldsymbol{x})$, which is a scalar containing contributions from the error-weighted model–measurement mismatch and the departure from the a priori values:

$$J(\boldsymbol{x}) = \frac{1}{2} \sum_{\boldsymbol{h}(\boldsymbol{x}) \in \Omega} (\boldsymbol{h}(\boldsymbol{x}) - \boldsymbol{y})^T \mathbf{S}_y^{-1} (\boldsymbol{h}(\boldsymbol{x}) - \boldsymbol{y}) + \frac{1}{2} (\boldsymbol{x} - \boldsymbol{x}_a)^T \mathbf{S}_a^{-1} (\boldsymbol{x} - \boldsymbol{x}_a), \quad (1)$$

where $\boldsymbol{x}$ is a vector of the parameters to be optimized (in this case, emission scaling factors), $\boldsymbol{x}_a$ contains the a priori values of those parameters, $\boldsymbol{y}$ is a set of observed $N_2O$ mixing ratios, $\boldsymbol{h}(\boldsymbol{x})$ is a vector containing the simulated mixing ratios at the time and location of each observation, $\mathbf{S}_y$ and $\mathbf{S}_a$ are the observational and a priori error covariance matrices, and $\Omega$ represents the time–space domain of the observations.

We use a quasi-Newtonian routine (Zhu et al., 1994; Byrd et al., 1995) to iteratively converge to $\min(J(\boldsymbol{x}))$. At each iteration, we use the adjoint of GEOS-Chem to compute the gradient of $J(\boldsymbol{x})$ with respect to the emission scaling factor and employ a lower bound of zero and an upper bound of 10 based on our earlier work (Wells et al., 2015). This approach therefore implicitly assumes that the sign of the a priori flux (which can be negative over the ocean) is correct for each model grid square. The GEOS-Chem adjoint has previously been applied to a wide range of inverse problems for atmospheric composition, including constraining sources and sinks of long-lived greenhouse gases such as $CO_2$ (Deng et al., 2014; Liu et al., 2014; Deng et al., 2015; Liu et al., 2015), methane (Wecht et al., 2014; Turner et al., 2015a), and $N_2O$ (Wells et al., 2015), as well as aerosols and reactive trace gases (e.g., Henze et al., 2007; Kopacz et al., 2009; Wells et al., 2014).

A priori uncertainties are assumed to be 100 % for both land and ocean emissions, with off-diagonal terms assuming correlation length scales of 500 and 1000 km, respectively, following prior work by Thompson et al. (2011, 2014a). Observational errors are calculated as the quadratic sum of measurement uncertainty ($\sim$ 0.4 ppb for most sites; see Sect. 2.4) and model transport uncertainty, with the latter estimated from the 3-D model variance in $N_2O$ mixing ratios in the grid boxes surrounding any given observation (resulting in a mean uncertainty $\sim$ 0.2 ppb at the surface). The corresponding mean observational uncertainty is $\sim$ 0.45 ppb, with maximum values $\sim$ 4 ppb. The solution presented here was calculated using 40 iterations, after which the cost function change per iteration is $< 1$ % and the total cost function reduction is $\sim$ 65 % (Fig. S2 in the Supplement).

#### 2.2.2 Continental-scale inversion

While the above approach avoids any aggregation error, the existing observational network provides insufficient information to constrain $N_2O$ emissions in every $4° \times 5°$ model grid square. Therefore, in an alternate inversion, we reduce the dimension of the inverse problem by solving for emission scaling factors on six continental (North America, South America, Europe, Africa, Asia, Oceania) and three ocean regions (northern oceans: 30–90° N; tropical oceans: 30° S–30° N; and southern oceans: 30–90° S). Regions are mapped in Fig. S1 in the Supplement and are similar to those used in the TransCom $N_2O$ model intercomparison study (Thompson et al., 2014b, c), except with one rather than two Asian regions. While this inversion could readily be carried out analytically rather than numerically (due to its small dimension), we instead use 4D-Var for consistency and to impose the same scaling factor bounds (0–10) as in the standard inversion. We thus use the GEOS-Chem adjoint to calculate the cost function gradient ($\nabla_{\boldsymbol{x}} J(\boldsymbol{x})$) aggregated over the nine predefined regions. We then iteratively minimize $J(\boldsymbol{x})$, achieving a cost function change of $< 1$ % per iteration (and total reduction of $\sim$ 55 %) after 28 iterations (Fig. S2 in the Supplement).

#### 2.2.3 SVD-based inversion

As an advance over standard aggregation methods such as the one described above, we also apply a new, efficient SVD-based information content analysis technique that maximizes the degrees of freedom of the inverse system while permitting us to solve for $N_2O$ fluxes in a fast iterative framework. The method, based on synthesis and advancement of recent work in this area (Flath et al., 2011; Bui-Thanh et al., 2012; Spantini et al., 2015) by Bousserez and Henze (2017), uses an optimal low-rank projection of the inverse problem that maximizes the observational constraints. Specifically, for a given dimension $k$, the optimal reduced space (Spantini et al., 2015; Bousserez and Henze, 2017) is spanned by the first $k$ eigenvectors of the prior-preconditioned Hessian $\mathbf{G}$ (Flath et al., 2011):

$$\mathbf{G} \equiv \mathbf{S}_a^{\frac{1}{2}} \mathbf{H}^T \mathbf{S}_y^{-1} \mathbf{H} \mathbf{S}_a^{\frac{1}{2}} = \mathbf{V} \boldsymbol{\Lambda} \mathbf{V}^T, \quad (2)$$

where $\mathbf{H}$ is the tangent linear of the forward model, $\mathbf{V}$ is a matrix whose columns are the eigenvectors of $\mathbf{G}$, and $\boldsymbol{\Lambda}$ is a diagonal matrix containing the eigenvalues of $\mathbf{G}$. The following analytical approximation can then be used:

$$\mathbf{S}_{\text{opt}} = \mathbf{S}_a - \mathbf{S}_a^{\frac{1}{2}} \left( \sum_{i=1}^{k} \frac{\lambda_i}{\lambda_i + 1} \boldsymbol{v}_i \boldsymbol{v}_i^T \right) \mathbf{S}_a^{\frac{1}{2}}, \quad (3)$$

where $\mathbf{S}_{\text{opt}}$ is the posterior error covariance matrix, while $\boldsymbol{v}_{i,i=1,\ldots,k}$ and $\lambda_{i,i=1,\ldots,k}$ are the eigenvectors and eigenval-

ues of $\mathbf{G}$. This expression gives, in some sense, the lowest error rank-$k$ approximation of $\mathbf{S}_{\text{opt}}$ (see Bousserez and Henze, 2017, for details). The eigenvectors $\boldsymbol{v}_i$ can be interpreted as the most constrained modes in flux space, i.e., flux patterns that are independently constrained by the observations (Cui et al., 2014; Bousserez and Henze, 2017). These eigenvectors of the prior-preconditioned Hessian are efficiently calculated using a fully parallelized randomized algorithm (Halko et al., 2011), as in Bui-Thanh et al. (2012) and Bousserez and Henze (2017). We use $k = 350$ here, which employs nearly all modes with eigenvalues greater than 1.0 (Fig. S3 in the Supplement), as modes with eigenvalues below this threshold are informed mainly by the prior.

From $\mathbf{S}_{\text{opt}}$ we can obtain the inversion averaging kernel ($\mathbf{AK}$), which gives a measure of how well emissions are constrained in a given location, as follows:

$$\mathbf{AK} = \mathbf{I} - \mathbf{S}_{\text{opt}}\mathbf{S}_a, \tag{4}$$

where $\mathbf{I}$ is the identity matrix and $\mathbf{S}_a$ is the a priori error covariance matrix. Optimized solutions in areas where the diagonal of $\mathbf{AK}$ is close to 1.0 are well constrained by the observations. The trace of the averaging kernel gives the total degrees of freedom, i.e., the number of independent pieces of information that can be obtained in the inversion framework.

The posterior mean estimate of $\boldsymbol{x}$ can also be directly calculated from analytical formulas using the eigenvectors of $\mathbf{G}$ (Spantini et al., 2015; Bouserez and Henze, 2017). However, to impose a positivity constraint on the emissions, we rely here on the variational minimization framework as in the standard 4D-Var case. In order to leverage the use of the optimal basis set, we project both the cost function and its gradient onto the principal modes to obtain a reduced analytical formulation. The analytical expression for the reduced cost function (derivation presented in Appendix A) is

$$\begin{aligned} J(\boldsymbol{x}) \approx & \frac{1}{2}(\boldsymbol{x}-\boldsymbol{x}_a)^T \mathbf{S}_a^{-\frac{1}{2}} \sum_{i=1}^{k} \boldsymbol{v}_i \boldsymbol{v}_i^T \mathbf{S}_a^{-\frac{1}{2}} (\boldsymbol{x}-\boldsymbol{x}_a) \\ & + \frac{1}{2}(\boldsymbol{h}(\boldsymbol{x}_a)-\boldsymbol{y})^T \mathbf{S}_y^{-1} (\boldsymbol{h}(\boldsymbol{x}_a)-\boldsymbol{y}) \\ & + \frac{1}{2}(\boldsymbol{x}-\boldsymbol{x}_a)^T \mathbf{S}_a^{-\frac{1}{2}} \sum_{i=1}^{k} \lambda_i \boldsymbol{v}_i \boldsymbol{v}_i^T \mathbf{S}_a^{-\frac{1}{2}} (\boldsymbol{x}-\boldsymbol{x}_a) \\ & + \frac{1}{2}(\boldsymbol{h}(\boldsymbol{x}_a)-\boldsymbol{y})^T \mathbf{S}_y^{-\frac{1}{2}} \sum_{i=1}^{k} \lambda_i^{\frac{1}{2}} \boldsymbol{w}_i \boldsymbol{v}_i^T \mathbf{S}_a^{-\frac{1}{2}} (\boldsymbol{x}-\boldsymbol{x}_a) \\ & + \frac{1}{2}(\boldsymbol{x}-\boldsymbol{x}_a)^T \mathbf{S}_a^{-\frac{1}{2}} \sum_{i=1}^{k} \lambda_i^{\frac{1}{2}} \boldsymbol{v}_i \boldsymbol{w}_i^T \mathbf{S}_y^{-\frac{1}{2}} (\boldsymbol{h}(\boldsymbol{x}_a)-\boldsymbol{y}), \end{aligned} \tag{5}$$

while the analytical approximation for the cost function gradient is

$$\begin{aligned} \nabla J(\boldsymbol{x}) \approx & \mathbf{S}_a^{-\frac{1}{2}} \sum_{i=1}^{k} \boldsymbol{v}_i \boldsymbol{v}_i^T \mathbf{S}_a^{-\frac{1}{2}} (\boldsymbol{x}-\boldsymbol{x}_a) \\ & + \mathbf{S}_a^{-\frac{1}{2}} \sum_{i=1}^{k} \lambda_i \boldsymbol{v}_i \boldsymbol{v}_i^T \mathbf{S}_a^{-\frac{1}{2}} (\boldsymbol{x}-\boldsymbol{x}_a) \\ & + \mathbf{S}_a^{-\frac{1}{2}} \sum_{i=1}^{k} \lambda_i^{\frac{1}{2}} \boldsymbol{v}_i \boldsymbol{w}_i^T \mathbf{S}_y^{-\frac{1}{2}} (\boldsymbol{h}(\boldsymbol{x}_a)-\boldsymbol{y}), \end{aligned} \tag{6}$$

where $k = 350$ is the number of modes retained in the approximation. Here, $\boldsymbol{h}(\boldsymbol{x}_a)$ are the model mixing ratios corresponding to the a priori emissions and $\boldsymbol{w}_i$ are the eigenvectors in observation space:

$$\boldsymbol{w}_i = \frac{1}{\sqrt{\lambda_i}} \mathbf{S}_y^{-\frac{1}{2}} \mathbf{H} \mathbf{S}_a^{\frac{1}{2}} \boldsymbol{v}_i. \tag{7}$$

Because the cost function and gradient depend only on the a priori model–measurement difference, the a priori and observational error covariances, and the eigenvectors of $\mathbf{G}$ (which are computed only once), this iterative inversion offers significant time savings, particularly for models with a low level of parallelization. Monthly $N_2O$ emission scaling factors for the 2-year analysis window are derived in approximately 6 h vs. over 100 h for the standard and continental-scale inversions, and nearly all the computation time in the former case is spent on calculating the eigenvectors of $\mathbf{G}$. The solution for the SVD-based inversion (with a projected cost function change of $< 1\,\%$ per iteration) is obtained after 60 iterations (Fig. S2 in the Supplement). The full cost function reduction (calculated from a forward model run) is $\sim 25\,\%$ for this solution, whereas we achieve the minimum in the full cost function at a much earlier iteration (see Fig. S2 in the Supplement). The divergence in the behavior of the projected and full cost function after this point may suggest that the weaker modes included here are not as well approximated by the randomized-SVD calculation as the dominant modes. An objective criteria for determining the error in the randomized SVD is the subject of a work in progress.

### 2.3 Atmospheric $N_2O$ observations

Atmospheric $N_2O$ observations used in our analysis include a global ensemble of surface measurements as well as airborne data from the HIAPER Pole-to-Pole Observations (HIPPO) campaigns (Wofsy, 2011). Because we found in our prior work that the surface dataset provides the strongest constraint on the spatial distribution of $N_2O$ emissions (Wells et al., 2015), we employ these in the inversion and reserve the airborne data for a posteriori evaluation.

Figure 1 shows a map of the surface measurement sites used in this study. The surface measurements consist primarily of discrete air-filled flasks from NOAA's Cooperative Global Air Sampling Network (CCGG) program (Dlugokencky et al., 1994); we also include flask-based air samples

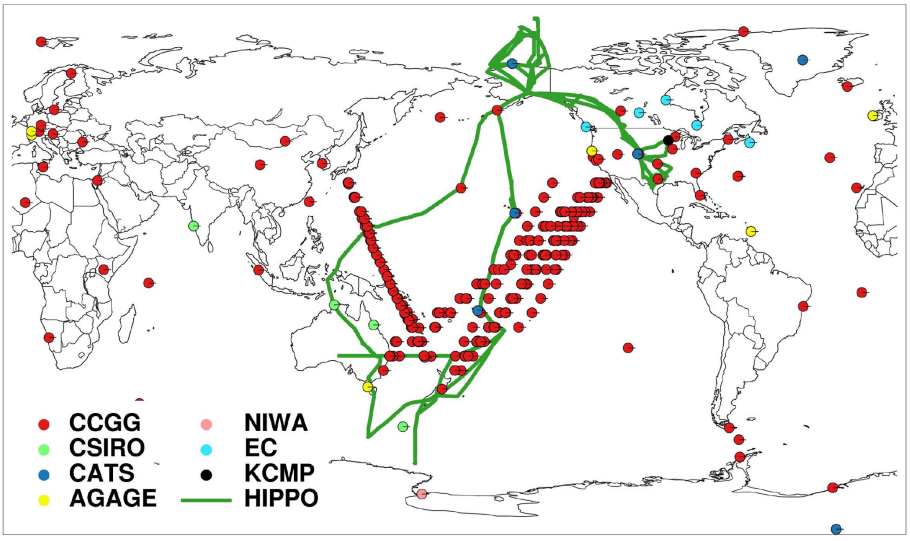


**Figure 1.** Global surface observing network for atmospheric $N_2O$. Shown are surface discrete measurement locations for the NOAA Carbon Cycle and Greenhouse Gases (CCGG) network, the Commonwealth Scientific and Industrial Research Organisation (CSIRO) network, the National Institute of Water and Atmospheric Research (NIWA) network, and the Environment Canada (EC) network, as well as semi-continuous measurement locations in the NOAA Chromatograph for Atmospheric Trace Species (CATS) network, the Advanced Global Atmospheric Gases Experiment (AGAGE) network, and the KCMP tall tower site. Also shown are flight tracks from the HIPPO IV and V deployments.

**Table 1.** The six initial conditions (for 1 April 2010) tested for $N_2O$, including the time range of observations used, observation sites included, interpolation or optimization method used, and length of spinup.

| Test name | Observational time range | Sites | Estimation method | Spinup |
|---|---|---|---|---|
| MarZonal | 1–31 Mar 2010 | All | Zonal average, linear interp | One month |
| AprZonal | 25 Mar–7 Apr 2010 | All | Zonal average, linear interp | None |
| AprKriging | 25 Mar–7 Apr 2010 | All | Kriging | None |
| AprOpt | 1 Apr–31 May 2010 | All | 4D-Var | None |
| FebOpt | 1 Feb–31 Mar 2010 | All | 4D-Var | Two months |
| RemoteOpt | 1 Jan–30 Jun 2010 | Remote[a] | 4D-Var | Three months |

[a] Remote sites include NOAA CCGG sites AZR, CBA, CGO, CHR, CRZ, DRP, GIC, GMI, HBA, ICE, IZO, MID, MLO, PSA, SEY, SHM, SUM, SYO, as well as ship-based measurements taken in the Pacific (POC).

from the Commonwealth Scientific and Industrial Research Organisation (CSIRO) network, the Environment Canada (EC) network, and a National Institute of Water and Atmospheric research (NIWA) site. We assume a measurement uncertainty of 0.4 ppb at all flask sampling sites based on recommendations from the data providers. In addition to the flask-based air samples, we use high-frequency $N_2O$ measurements (discrete hourly or hourly averaged) from the NOAA Chromatograph for Atmospheric Trace Species (CATS) network (Hall et al., 2007), the Advanced Global Atmospheric Gases Experiment (AGAGE) network (Prinn et al., 2000), and the University of Minnesota tall tower (KCMP tall tower; Griffis et al., 2013; Chen et al., 2016). The hourly measurement uncertainty at these sites is approximately 0.3, 0.6, and 1 ppb, respectively.

Small calibration offsets between measurement networks can significantly impact $N_2O$ inversions due to its low ambient variability relative to background mixing ratios. To address this, we adjust here the AGAGE and EC data to the same NOAA 2006A scale used by the NOAA CCGG, CATS, CSIRO, NIWA, and KCMP measurements. For AGAGE, we calculate an adjustment factor based on co-located CCGG flask-based air samples taken within 15 min of an in situ measurement at five sites: CGO (Cape Grim, Australia), MHD (Mace Head, Ireland), RPB (Ragged Point, Barbados), SMO (Tutuila, American Samoa), and THD (Trinidad Head, California). The mean CCGG : AGAGE ratio at these sites from 2010 to 2012 is 1.00037, and we apply this adjustment to all AGAGE data. For EC, we calculate an adjustment factor based on co-located NOAA flask-based air measurements at ALT (Alert, Nunavut, Canada). The mean NOAA : EC ratio

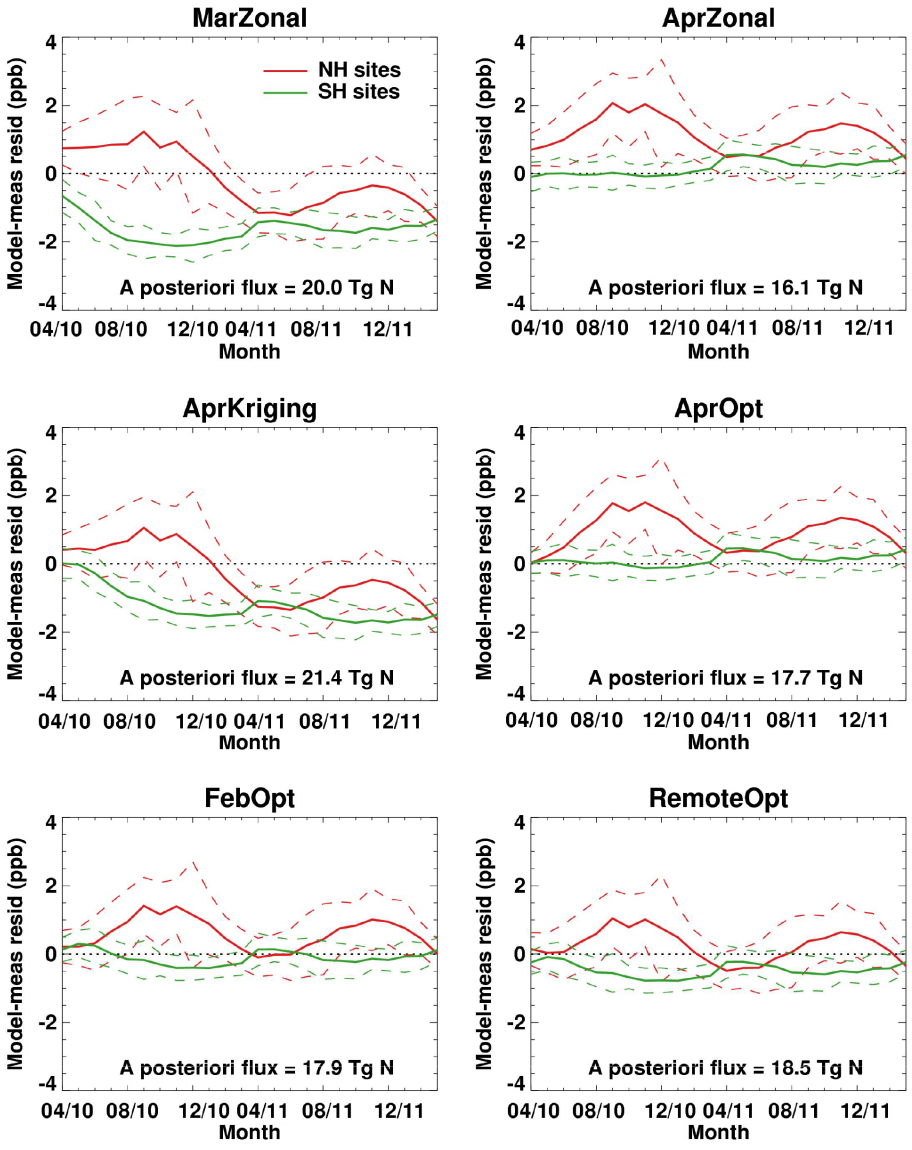


**Figure 2.** Impact of initial conditions on a 2-year (April 2010–April 2012) $N_2O$ simulation and inversion. Shown are timelines of the model–measurement residuals for a 2-year forward model simulation initialized using each of the six initial conditions listed in Table 1. The solid line represents the mean and the dashed lines represent the standard deviation about the mean for Northern Hemisphere (red) and Southern Hemisphere sites (green). The final 2011 a posteriori global flux for each simulation derived using a standard 4D-Var inversion is noted at the bottom of each panel.

during our analysis period is 1.00017, and we use this adjustment factor across the EC network. While calibration-scale offsets can be concentration and time dependent, our relatively short (2-year) analysis window avoids the need for any temporally resolved measurement adjustments. Prior to our analysis we also screen for outliers by omitting any measurements more than 2 standard deviations (calculated on a running basis with a 30-day time window for flask-based air measurements and a 24 h time window for in situ observations) away from its nearest neighbor.

For a posteriori evaluation of the inverse modeling results we employ airborne measurements from the HIPPO campaigns (Wofsy, 2011), which featured pole-to-pole sampling and regular vertical profiling from approximately 300 to 8500 m altitude, with some profiles extending to 14 000 m. Figure 1 shows flight tracks for the two deployments occurring during our simulation period and used here: HIPPO IV (June–July 2011) and HIPPO V (August–September 2011). The aircraft payload included high-frequency $N_2O$ measurements by quantum cascade laser spectroscopy (Kort et al., 2011). To ensure calibration consistency we apply an offset adjustment to these data for each deployment based on concurrent flask-based air samples, which are anchored to the NOAA 2006A scale.

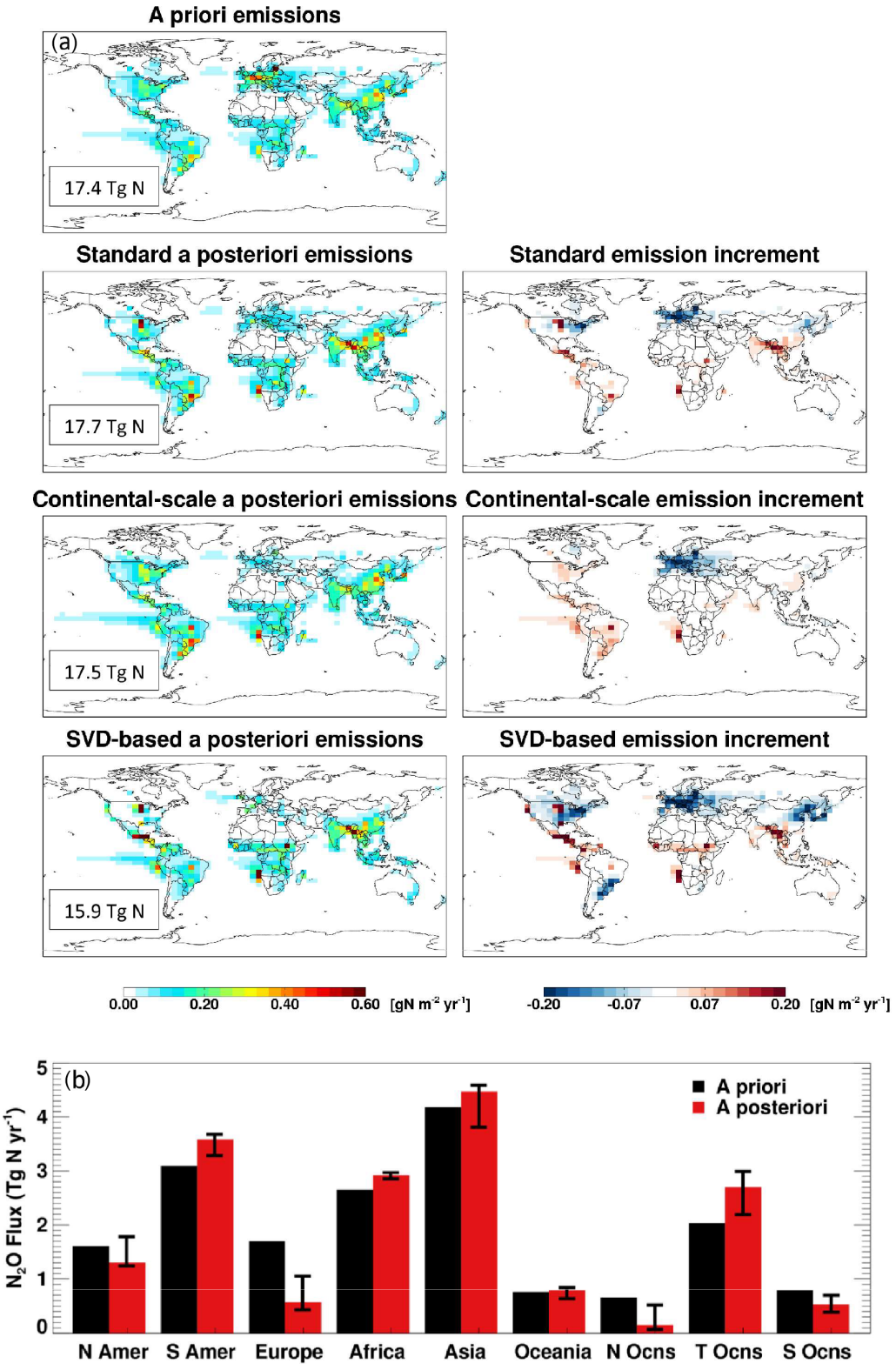


**Figure 3. (a)** Left panels: 2011 annual $N_2O$ emissions for the a priori database and a posteriori results for each of the inversion frameworks used here (standard 4D-Var, continental-scale inversion, SVD-based inversion). Global fluxes are shown inset in each map. Right panels: annual posterior emission increments relative to the a priori database for each inversion framework. **(b)** 2011 annual $N_2O$ flux over six continental and three oceanic regions for the a priori database (black) and the a posteriori median from the three inversion frameworks (red). Error bars denote the range of a posteriori values for each region.

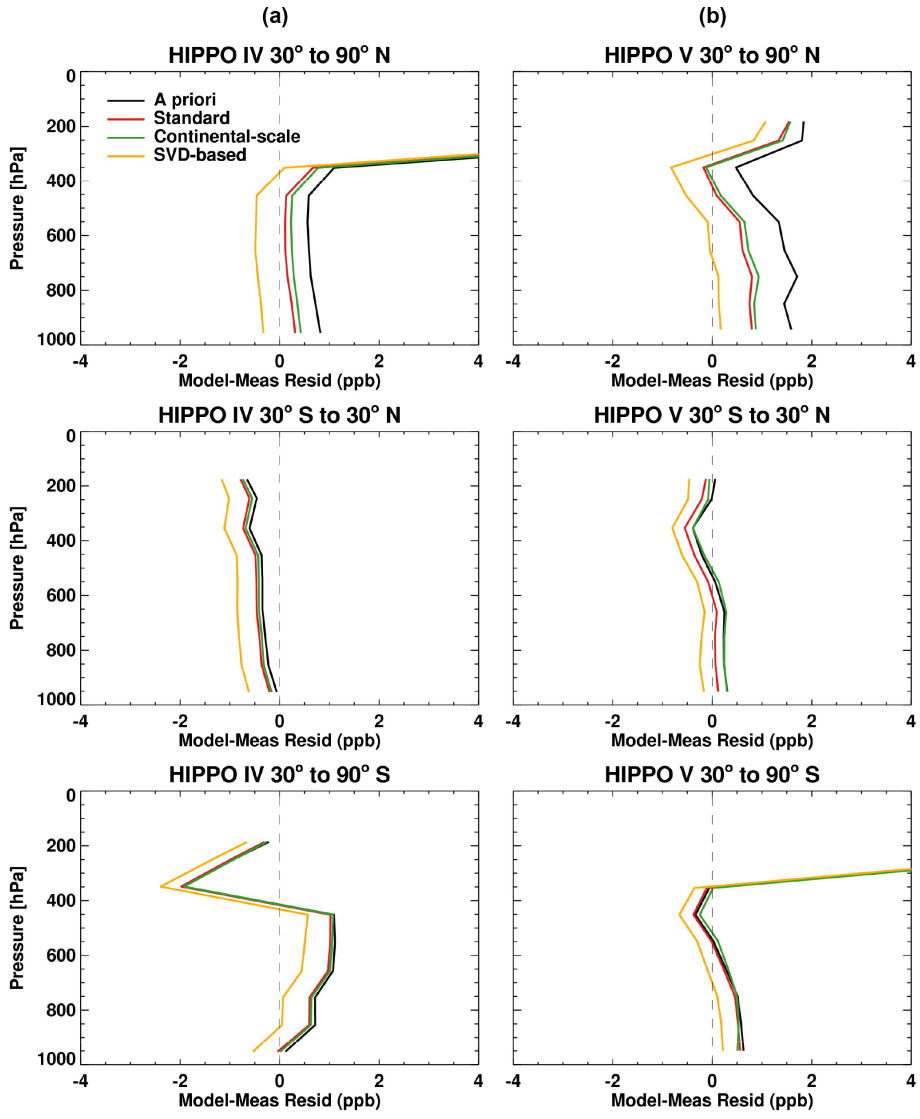


**Figure 4.** A posteriori evaluation of $N_2O$ inversion results using HIPPO data (not themselves used in the inversion). Shown are mean vertical profiles of the model–measurement difference for HIPPO IV **(a)**, 14 June–11 July 2011 and HIPPO V **(b)**, 9 August–9 September 2011 as a function of latitude. A priori results are shown in black and a posteriori results in red (standard 4D-Var inversion), green (continental-scale inversion), and gold (SVD-based inversion).

## 3 Inversion sensitivity to initial conditions for $N_2O$

Because of the ∼ 127-year atmospheric lifetime for $N_2O$, any bias in the model initial conditions can persist throughout the analysis period and lead to substantial errors in top-down emission estimates (Thompson et al., 2014c). In this section, we evaluate six alternate approaches to generating initial $N_2O$ mass fields for the start date of our inversions (1 April 2010), their impact on the derived fluxes, and their overall suitability for inverse modeling.

The six treatments are summarized in Table 1. Three involve interpolation of surface observations from the NOAA, AGAGE, CSIRO, EC, and NIWA networks for alternate time windows (MarZonal, AprZonal, AprKriging), two involve 4D-Var adjoint optimization of the initial mass field based on those same observations plus those from KCMP tall tower (AprOpt, FebOpt), and one involves optimization of the initial mass field based on observations from remote sites (RemoteOpt). Interpolation of observations offers the advantage of avoiding any model information that may bias the initial state, whereas a 4D-Var optimization of the initial conditions allows us to exploit subsequent atmospheric transport to inform the initial state in locations without $N_2O$ observations. The first three approaches employ either linear interpolation of zonally averaged surface measurements or kriging, and use observations from March 2010 (with subsequent 1-month model spinup) or from 25 March to 7 April 2010 (with

no subsequent spinup). In each case, the resulting surface mixing ratios of $N_2O$ (mapped in Fig. S4 in the Supplement) are assigned to all vertical levels in the troposphere; initial $N_2O$ mixing ratios above 100 hPa are based on interpolated mean profiles from the EOS Aura Microwave Limb Sounder (MLS; Lambert et al., 2007). Where necessary, $N_2O$ mixing ratios above the tropopause but below 100 hPa are linearly interpolated between the tropospheric and MLS values.

The three tests in which the initial conditions are optimized by 4D-Var use a time window of February–March 2010, April–May 2010, or January–June 2010 to solve for the initial $N_2O$ mass field on 1 April 2010. Two of these assimilate all surface observations while one employs only data from remote sites. Below, we evaluate each of the six initial condition treatments against observations at the beginning of the simulation period (1–7 April 2010) and perform a standard 4D-Var optimization of $N_2O$ emissions to quantify the sensitivity of the inferred fluxes to the selected initial conditions.

Table 2 shows initial bias statistics with respect to all surface observations and by hemisphere for each initial condition treatment. Of the interpolation approaches, the MarZonal setup has the poorest performance, with an overly strong interhemispheric gradient (the model is biased high in the Northern Hemisphere and low in the Southern Hemisphere) and the largest initial model–measurement bias at all sites. In this case, the 1-month model spinup, meant to smooth out any artificial $N_2O$ gradients from the interpolation, is counterproductive as it allows model emission biases to accumulate prior to the inversion. The interpolation methods without subsequent spinup (AprZonal, AprKriging) perform better in terms of initial model–measurement bias – in the global mean and in each individual hemisphere. We see the same general behavior when using 4D-Var to optimize the initial conditions, with the no-spinup AprOpt approach providing the lowest initial model–measurement bias (and least spread in bias) across all of the six methods tested. Using only data from remote sites (RemoteOpt) in the initial field optimization leads to a negative model bias, on average, in both hemispheres.

The bias statistics above can only test the realism of the initial $N_2O$ fields in those locations where there are observations, but say nothing about any potential bias in the large majority of model grid squares that lack observations. However, by carrying out a full forward model run based on each of those initial conditions, we can exploit atmospheric transport to more fully assess the fidelity of the initial $N_2O$ mass field based on the evolution of model–measurement biases at the various observation sites.

Figure 2 shows monthly-mean model–measurement residuals (averaged for Northern and Southern Hemisphere sites) for a full 2-year forward simulation using the a priori emissions for each of the above initial mass fields. While most of the initial conditions exhibit minimal bias at the start of the simulation, some develop large biases over time. As a result, the corresponding a posteriori global flux obtained in a 4D-Var source inversion (values shown inset in Fig. 2) varies considerably depending on the initial $N_2O$ field, with the flux adjustment even changing sign: a posteriori values range from 16.1 to 21.4 $\mathrm{Tg\,N\,yr^{-1}}$, i.e., from a $\sim 7\,\%$ reduction to a 23 % increase in the prior flux. We see in Fig. 2 that the direction of the global flux adjustment corresponds to the trend in the model–measurement residuals. For example, with the MarZonal initial conditions, a significant negative trend in the residuals drives a global flux increase relative to the a priori, despite the fact that this case exhibits a positive mean bias with respect to the observations at the outset (Table 2). Such a trend in the model–measurement residuals could theoretically arise from the accumulation of model source–sink errors over the course of the simulation. However, our a priori flux and lifetime are broadly consistent with independent observational constraints (Prather et al., 2012), whereas an annual $N_2O$ source of 20+ Tg N would yield a higher-than-observed atmospheric growth rate. A biased initial mass field is thus the more tenable explanation for the negative model–measurement residual trend.

Overall, the three simulations using initial conditions optimized by 4D-Var yield a relatively small trend in the model–measurement $N_2O$ residuals, as does the AprZonal simulation, arguing for a more realistic initial $N_2O$ distribution in these cases. While the a posteriori flux between them varies, differences are less than 10 % of the a priori flux. Because the AprOpt initial conditions exhibit the lowest initial bias, along with the lack of a trend in the residual timeline, we choose this method to construct the initial conditions for the $N_2O$ inversions presented here. Likewise, for future work on $N_2O$ and other long-lived species, we recommend constructing the initial conditions by 4D-Var assimilation of observations at the outset of the inversion period. Because they are used for initial condition optimization, the April–May 2010 surface observations are excluded from the subsequent source inversions.

## 4 Inversion evaluation and results

Figure 3 shows maps of our derived annual a posteriori $N_2O$ emissions from the standard, continental-scale, and SVD-based inversion for 2011, along with bar charts of the 2011 annual flux for the nine regions considered in the continental-scale inversion (numerical values listed in Table 3). A priori emissions, along with a posteriori emission increments (a posteriori–a priori difference) are also included for comparison. We focus on 2011 results to minimize any residual bias from the initial conditions. Focusing on 2011 also excludes the last 3 months of the inversion window when the adjoint forcing weakens due to the long lifetime of $N_2O$ (Wells et al., 2015).

The optimized global fluxes, listed inset in each map in Fig. 3, range from 15.9 $\mathrm{Tg\,N\,yr^{-1}}$ for the SVD-based inver-

**Table 2.** Initial bias statistics for each of the six initial conditions with respect to observations at all sites, Northern Hemisphere sites, and Southern Hemisphere sites. Statistics are calculated for the first week of the simulation (1–7 April 2010).

| | Bias: all sites (ppb) | | | Bias: Northern Hemisphere sites (ppb) | | | Bias: Southern Hemisphere sites (ppb) | | |
|---|---|---|---|---|---|---|---|---|---|
| Test name | 25th | Median | 75th | 25th | Median | 75th | 25th | Median | 75th |
| MarZonal | −0.21 | 0.30 | 0.71 | 0.11 | 0.46 | 0.86 | −0.66 | −0.36 | −0.15 |
| AprZonal | −0.13 | 0.20 | 0.62 | −0.03 | 0.32 | 0.73 | −0.38 | −0.12 | 0.10 |
| AprKriging | −0.29 | 0.06 | 0.42 | −0.31 | 0.02 | 0.39 | −0.20 | 0.14 | 0.49 |
| AprOpt | −0.21 | 0.01 | 0.21 | −0.22 | 0.01 | 0.20 | −0.21 | 0.01 | 0.22 |
| FebOpt | −0.29 | 0.06 | 0.48 | −0.42 | −0.03 | 0.37 | −0.16 | 0.14 | 0.39 |
| RemoteOpt | −0.48 | −0.14 | 0.22 | −0.44 | −0.09 | 0.33 | −0.58 | −0.30 | −0.04 |

**Table 3.** 2011 $N_2O$ emissions ($Tg\,N\,yr^{-1}$) over six continental and three oceanic regions for the a priori database and a posteriori results for the three inversion frameworks used here.

| | | A posteriori emissions | | |
|---|---|---|---|---|
| Region | A priori emissions | Standard 4D-Var inversion | Continental-scale inversion | SVD-based inversion |
| North America | 1.61 | 1.30 | 1.78 | 1.24 |
| South America | 3.09 | 3.68 | 3.58 | 3.28 |
| Europe | 1.70 | 1.05 | 0.57 | 0.43 |
| Africa | 2.65 | 2.97 | 2.92 | 2.85 |
| Asia | 4.18 | 4.47 | 4.59 | 3.81 |
| Oceania | 0.76 | 0.79 | 0.64 | 0.84 |
| Northern oceans (30–90° N) | 0.66 | 0.52 | 0.07 | 0.15 |
| Tropical oceans (30° S–30° N) | 2.03 | 2.19 | 2.99 | 2.70 |
| Southern oceans (30–90° S) | 0.79 | 0.70 | 0.39 | 0.53 |
| Global | 17.4 | 17.7 | 17.5 | 15.9 |

sion to 17.5–17.7 $Tg\,N\,yr^{-1}$ for the standard and continental-scale inversions, with some similar spatial patterns and some discrepancies that we explore further in Sect. 4.3. The SVD-based global flux agrees well with that implied by the $N_2O$ lifetime and global burden for 2010 ($15.7 \pm 1.1\,Tg\,N\,yr^{-1}$; Prather et al., 2012). It also gives a better comparison to HIPPO IV and V measurements in the southern extratropics and to HIPPO V in the northern extratropics (see below). However, all three a posteriori global annual fluxes are close to or within the range of recent inverse studies (16.1–18.7 $Tg\,N\,yr^{-1}$). Below we evaluate our inversion results using aircraft observations before interpreting them in terms of the information they provide on $N_2O$ emission processes.

### 4.1 A posteriori evaluation of $N_2O$ emissions

We apply the HIPPO IV and V airborne measurements described in Sect. 2.3 (and mapped in Fig. 1) to evaluate the a posteriori fluxes from our different inversion methods and assess which method yields the most realistic depiction of true $N_2O$ fluxes. Figure 4 shows average vertical profiles of the model–measurement $N_2O$ difference for these deployments in the a priori and the three inverse estimates as a function of latitude. Initially, the model vertical profile is biased high throughout the troposphere in the northern mid-to-high latitudes; this bias is larger during HIPPO V than HIPPO IV due to a seasonal bias in model emissions that is further discussed in Sect. 4.4. In the southern mid-to-high latitudes the model is also biased high through most of the troposphere. In most cases in Fig. 4 we see that the model–measurement difference trends negative with height in the troposphere, which may reflect a model underestimate of the convective transport of $N_2O$ emissions (Kort et al., 2011). Large biases above 400 hPa in HIPPO IV (30–90° N) and HIPPO V (30–90° S) are driven by high-latitude observations in which the aircraft is sampling below the model tropopause but above the actual tropopause and highlight the difficulty in modeling the $N_2O$ vertical profile at these altitudes.

All three inversions significantly reduce the 30–90° N bias seen for both HIPPO campaigns; the SVD-based approach provides the fullest correction during HIPPO V, while slightly overcorrecting the HIPPO IV bias. However, the high bias from 30 to 90° S is only reduced in the SVD-based inversion despite the fact that the continental-scale inversion has the lowest a posteriori emissions in this latitude range (Ta-

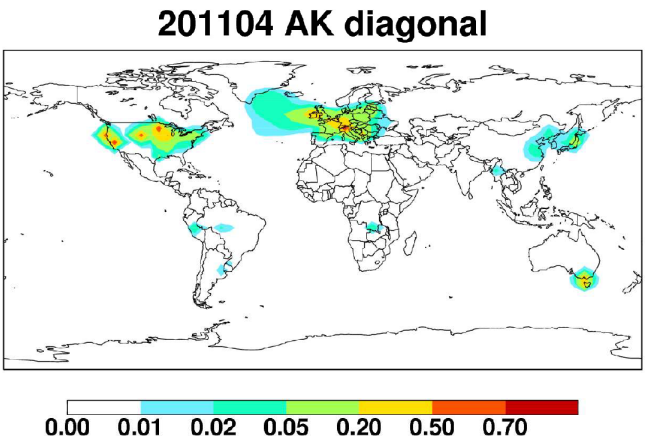


**Figure 5.** Averaging kernel diagonal values for April 2011 in the SVD-based inversion, calculated from Eq. (4).

ble 3). The lower global flux obtained with the SVD-based approach (Fig. 3 and Table 3) is thus the reason for this correction, implying that the global annual a priori flux (from all sources combined) may be too high. We note that a slight low bias does emerge in the tropics in the SVD-based approach, where observational constraints are low.

### 4.2 Averaging kernel

The information from the randomized-SVD algorithm can be used to directly calculate the inversion AK and posterior error via Eqs. (3) and (4), giving valuable information on the spatial distribution of emission constraints provided by the $N_2O$ observing network. Figure 5 shows the diagonal of the AK for $N_2O$ emissions in April 2011 (results for other months are very similar). AK diagonal values near 1.0 indicate emission locations that are well constrained by observations, while AK diagonal values close to 0 indicate emission locations that lack a direct constraint.

AK diagonal values for monthly $N_2O$ emissions are highest in the USA and Europe, where the observational coverage is most extensive, with values up to 0.7 in locations where hourly observations are available. Weaker constraints are achieved in East Asia and some tropical and Australian grid boxes, with AK values ranging from 0.01 to 0.4. AK values throughout most of the Tropics, Southern Hemisphere, Canada, and northern Asia reveal almost no direct observational constraints on monthly emissions in these regions.

The number of pieces of information that can be independently resolved (DOFs) in any inversion can be determined from the trace of the AK. Here, the DOFs are $\sim$ 315 for the full 2-year inversion. A key advantage of the SVD-based approach is that it solves for only those spatiotemporal flux patterns that can be constrained by the observations: i.e., the dimension of the solution is consistent with the DOFs of the inversion. In contrast, the standard inversion attempts to resolve 79 466 free variables, $\sim$ 250$\times$ more than can legitimately be constrained, while the continental-scale inversion yields fewer pieces of information (216) than are obtainable. The latter point confirms that the observations can in fact resolve some finer-scale spatial and temporal information on $N_2O$ emissions in the regions where AK values are highest.

### 4.3 Regional annual $N_2O$ emissions

In this section we interpret the inversion results by region in terms of their implications for present understanding of $N_2O$ emission processes. We focus on the spatial information obtained from the standard and SVD-based inversions and on those features that are most robust across these inversion frameworks.

#### 4.3.1 North America

A posteriori emissions from North America range from 1.24 to 1.78 Tg N yr$^{-1}$, with a slight increase (11 %) inferred relative to the a priori inventory for the continental-scale inversion vs. a 20–23 % decrease for the standard and SVD-based inversion. The latter values are quite close to a recent estimate from Saikawa et al. (2014) for 2008 ($1.2 \pm 0.2$ Tg N yr$^{-1}$). Both the standard and SVD-based inversions call for a large increase (2–3$\times$) in emissions from the US Corn Belt (Fig. 3), one of the most intensively managed agricultural regions of the world. The magnitude of this upward adjustment supports emission underestimates previously found for this region (Kort et al., 2008; Miller et al., 2012; Griffis et al., 2013), which have been attributed to underrepresentation of indirect $N_2O$ emissions following leaching and runoff from agricultural soils (Turner et al., 2015b; Chen et al., 2016). However, other processes could also contribute, such as freeze–thaw emissions or direct emissions after spring fertilizer application. The timing of these processes, and that of peak stream flow, corresponds to the dominant modes of ambient $N_2O$ variability observed in this region (Griffis et al., 2017). Finally, we find that emissions decrease relative to the a priori estimate in the western USA and Canada (in both the standard and SVD inversions), where natural soil emissions may be too high in the CLMCN-$N_2O$ inventory (Saikawa et al., 2014) used here, and where recent work argues that direct agricultural emissions are overestimated using a standard linear emission model (Gerber et al., 2016).

#### 4.3.2 South America

A posteriori emissions from South America range from 3.28 to 3.68 Tg N yr$^{-1}$, increasing 6–19 % over the a priori. These values are 40–60 % larger than the median inferred by Thompson et al. (2014c) for 2006–2008 (2.33 Tg N yr$^{-1}$); however, due to weak observational constraints (Fig. 5) we find that the results here are quite sensitive to the inversion framework used. For example, including fewer modes in the SVD-based solution yields an even higher a posteriori flux

in this region, and the spatial distribution of emissions differs substantially between the standard and SVD-based solutions. Saikawa et al. (2014) do note a large recent increase in nitrogen fertilizer consumption over this region (49 % from 1995 to 2008), which may help explain the larger a posteriori flux seen here, although N fertilizer use in this region was only 7 % of the global total in 2011 (International Fertilizer Association, 2016).

#### 4.3.3 Europe

All three inversions point to a significant model overestimate of European $N_2O$ emissions, with a posteriori fluxes that are 38 % (standard inversion; optimized flux $1.05\,\mathrm{Tg\,N\,yr^{-1}}$) to 75 % (SVD-based inversion; optimized flux $0.43\,\mathrm{Tg\,N\,yr^{-1}}$) lower than the a priori. These optimized fluxes are in better agreement with the other top-down flux estimates for Europe (both for 2006) of $1.19\,\mathrm{Tg\,N\,yr^{-1}}$ (Corazza et al., 2011) and $0.93 \pm 0.12\,\mathrm{Tg\,N\,yr^{-1}}$ (Saikawa et al., 2014). The European source derived in the SVD-based and continental-scale inversions ($0.43$–$0.57\,\mathrm{Tg\,N\,yr^{-1}}$) represents $\sim 3$ % of the global flux found in each case, which agrees with the result from Huang et al. (2008). We find the largest emission reductions over western and central Europe, suggesting an overestimate of soil and nonagricultural anthropogenic sources in the EDGARv4.2 inventory used here. While nonagricultural anthropogenic sources make up only $\sim 10$ % of the global a priori $N_2O$ flux, they comprise $\sim 30$ % of the European a priori model emissions. Based on the spatial distribution of the adjustments derived in the inversions, we find that both of these sources (soils, nonagricultural anthropogenic) have a comparable high bias (from 40 to 70 % as indicated by the standard and SVD-based inversions, respectively) in the a priori inventories over Europe.

#### 4.3.4 Africa

Annual emissions from Africa range from 2.85 to $2.97\,\mathrm{Tg\,N\,yr^{-1}}$ in all three inversions, an 8–12 % increase from the prior flux. Our a posteriori values are closer to the median optimized African flux found by Thompson et al. (2014c) for 2006–2008 ($3.36\,\mathrm{Tg\,N\,yr^{-1}}$) than is the a priori; however, the lack of direct observational constraints for this region (Fig. 5) prevents any definitive conclusion. As in South America, the SVD-based result here is quite sensitive to the number of modes used, with emission increments differing in sign for some months. The spatial distribution between the standard and SVD-based solutions also differs, with the former preserving the a priori distribution and the latter placing more of the flux in equatorial Africa.

#### 4.3.5 Asia

Over Asia the a posteriori flux ranges from $3.82\,\mathrm{Tg\,N\,yr^{-1}}$ (9 % decrease from the a priori) to $4.59\,\mathrm{Tg\,N\,yr^{-1}}$ (10 % increase). The full-dimensional and SVD-based inversions both call for a reduction in model emissions for northern China and Russia and an increase to the south. Consistent a posteriori spatial patterns emerge in the latter region, with large emission increases over the prior for the Indo-Gangetic Plain of India, Southeast Asia, and eastern China. Our flux estimates are towards the higher end of the wide range of estimates for North and South Asia ($2.87$–$4.48\,\mathrm{Tg\,N\,yr^{-1}}$) reported by Thompson et al. (2014c) for 2006–2008; that study concludes that observational constraints are low in this region, which is generally consistent with our findings (Fig. 5). Saikawa et al. (2014) find that agricultural $N_2O$ emissions are increasing in South Asia, and that is consistent with our higher flux for 2011 compared to the Thompson et al. (2014c) median value for 2006–2008. Of the total global N fertilizer consumption, 58 % occurred in South and East Asia in 2011 (International Fertilizer Association, 2016); it is possible that direct on-field $N_2O$ emissions here are underestimated with N inputs exceeding crop demands (Shcherbak et al., 2014). Indeed, a recent bottom-up estimate derives a direct emission response for China that is 42 % larger than the global average (Gerber et al., 2016). Over northern Asia our results point to an overestimate of natural soil emissions (as this is the dominant regional source in the model); a similar overestimate was inferred by Saikawa et al. (2014).

#### 4.3.6 Oceania

The emission estimates for Oceania range from $0.64\,\mathrm{Tg\,N\,yr^{-1}}$ (16 % decrease from the prior) to $0.84\,\mathrm{Tg\,N\,yr^{-1}}$ (10 % increase). Observational constraints are low in this region (outside of Cape Grim, where a measurement site exists; Fig. 5) and results depend strongly on the a priori. The weak emission reduction in the continental-scale inversion (Table 3) could also reflect a model overestimate of the southern ocean source, as the sparse observations make it difficult to separate land vs. ocean emissions here.

#### 4.3.7 Ocean emissions

We obtain an annual flux ranging from 0.07 to $0.52\,\mathrm{Tg\,N\,yr^{-1}}$ for northern oceans (30–90° N), 2.19 to $2.99\,\mathrm{Tg\,N\,yr^{-1}}$ for tropical oceans (30° S–30° N), and 0.39 to $0.70\,\mathrm{Tg\,N\,yr^{-1}}$ for southern oceans (30–90° S). In all cases, our results indicate an emission increase for tropical ocean emissions (of 9–47 %) and a decrease for northern (20–90 %) and southern (11–51 %) oceans relative to the a priori Jin and Gruber (2003) inventory. The wide range of values reflects the limited degree to which the surface observing network can constrain ocean emissions. However, the standard and SVD-based inversions both point to a model overestimate in the North Atlantic where downwind observations in Europe have some power to resolve monthly emissions.

The direction of the oceanic emission changes is consistent with the findings of Thompson et al. (2014c); however, our oceanic fluxes are lower than obtained in that study (1.08, 3.66, and 1.20 $Tg\,N\,yr^{-1}$ for northern, tropical, and southern oceans, respectively). Compared to Thompson et al. (2014c), results obtained here (3.38–3.45 $Tg\,N\,yr^{-1}$) are closer to the most recent best estimate of the oceanic source derived from observations of the air–sea $N_2O$ gradient ($2.4 \pm 0.8\,Tg\,N\,yr^{-1}$; Buitenhuis et al., 2017), albeit still higher. We find that ocean emissions make up $\sim 20\,\%$ of the global $N_2O$ flux (in both the a priori and a posteriori estimates), lower than found in some inverse studies (31–38 %; Saikawa et al., 2014; Thompson et al., 2014c) but consistent with Huang et al. (2008) ($\sim 23\,\%$).

#### 4.3.8 Summary of regional-scale results

Among the most robust spatial features of our results across all the inversion frameworks employed is an increase in annual $N_2O$ emissions over the a priori in the tropics (particularly 0–30° N) and a decrease at higher latitudes for both ocean and terrestrial sources. While the total Asian flux differs between the full-dimensional and SVD-based inversion, both solutions indicate a model overestimate in northern Asia and an underestimate in Southeast Asia. Furthermore, while the inversions disagree on whether the a priori emissions are too high or too low over North America as a whole, both the full-dimensional and SVD-based inversions increase the prior $N_2O$ emissions over the US Corn Belt and reduce them over the western USA and Canada. This suggests that while the a priori emissions may be too high in northern mid-to-high latitudes overall (which we attribute to overly high natural soil emissions in the model, as well as nonagricultural anthropogenic emissions in regions such as Europe, and a possible overestimate of direct emissions in drier regions), they are underestimated for fertilized agricultural soils in the US Corn Belt and likely also in Asia.

### 4.4 Seasonality of $N_2O$ emissions

#### 4.4.1 A priori seasonality

Figure 2 shows that the a priori model bias in atmospheric $N_2O$ varies strongly as a function of season in the Northern Hemisphere, implying a corresponding seasonal bias in the bottom-up emissions driving the model. Because the EDGARv4.2 emissions used here are annual, the seasonality in our prior emissions over land is dominated by the natural soil source. Here, we compare the temporal constraints afforded by the different inversions, focusing again on the most robust features across the inversions, after first examining the seasonality differences between modeled and measured $N_2O$ mixing ratios.

Figure 6 shows 2-year timelines of monthly-averaged a priori modeled and measured $N_2O$ mixing ratios along with the corresponding model–measurement residual for all surface measurement sites. The modeled $N_2O$ from 30 to 90° N is characterized by a November–December peak and a May–June minimum. This is out of phase with the measurements, which have a minimum around August–September and a peak in February–March. Several other CTMs in a recent intercomparison (Thompson et al., 2014b, c) likewise produce a seasonal minimum that is too early compared to observations, which that study suggests may reflect an overestimate of the impact of $N_2O$-depleted stratospheric air on surface mixing ratios. Our previous work indicates that surface $N_2O$ mixing ratios are not sensitive to biases in the magnitude of the stratospheric sink on the timescale of our inversion (Wells et al., 2015), while Thompson et al. (2011) find that errors in modeled stratosphere–troposphere exchange can bias inferred regional emissions by up to 25 %, particularly over the North Atlantic and Europe. We thus focus here on inferred seasonal changes that are significantly larger than 25 % and most robust to any potential errors in modeled stratosphere–troposphere exchange.

Measured mixing ratios at the KCMP tall tower site in Minnesota are significantly higher than other Northern Hemisphere sites. As a result, it is one of the few sites where negative model–measurement residuals persist through most of the 2-year inversion period. Located in an agricultural region composed mainly of drained lands, the low model bias is consistent with previous findings of a missing or strongly underestimated agricultural $N_2O$ source tied to indirect emissions (Griffis et al., 2013; Chen et al., 2016).

#### 4.4.2 Seasonality of $N_2O$ inversion results

Figure 7 contains 2011 timelines of the monthly a priori and a posteriori emissions for the three inversion methods over the same continental and ocean regions considered above. Both North American and European a posteriori emissions are characterized by a shift from a summertime (June–July) to springtime peak in emissions (March–April), with the North American results exhibiting separate spring and summer peaks (plus an October enhancement in the SVD-based inversion). The a posteriori seasonality over Asia is nearly reversed from the a priori, with dual emission peaks in spring (March–May) and fall (September–October). This double maximum is consistent with past work and coincides with the approximate start and end times of the Asian monsoon (Thompson et al., 2014c). Over South America and Africa we find that the a posteriori seasonality depends more strongly on the inversion method used, reflecting the low observational constraints in these regions (Fig. 5). Tropical ocean emissions increase primarily during summer and fall when emissions are at their peak, though the magnitude varies across inversion frameworks. Emissions decrease strongly for the northern oceans (though they were not large to begin with) for the continental and SVD-based inversions, but with no shift in seasonality. Seasonal emission adjust-

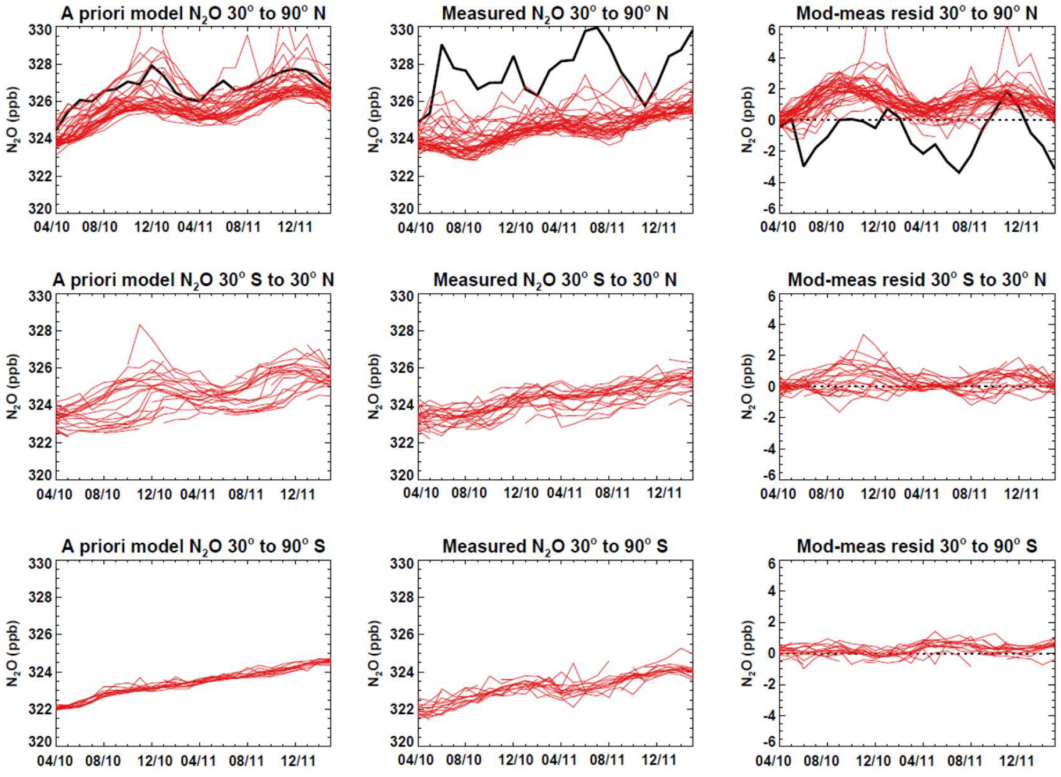


**Figure 6.** Two-year timelines of monthly-averaged a priori modeled and measured $N_2O$ mixing ratios, and the resulting model–measurement residuals, for individual measurement sites as a function of latitude. The solid black line in the top panels shows results for the KCMP tall tower site in MN, USA.

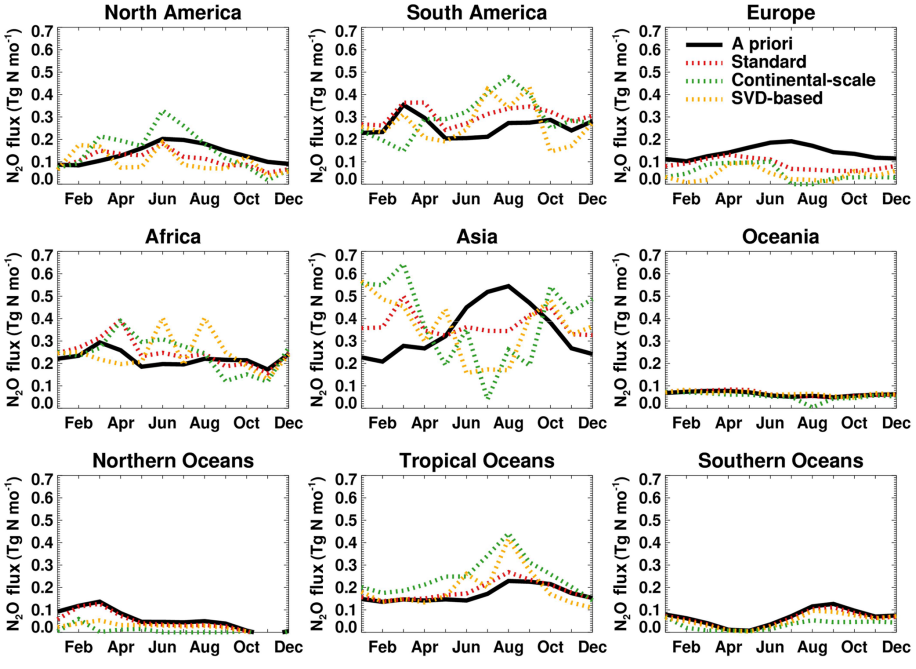


**Figure 7.** Monthly $N_2O$ emissions for 2011 over six continental and three oceanic regions. Shown is the a priori database (black) and a posteriori results for the standard 4D-Var inversion (red), the continental-scale inversion (green), and the SVD-based inversion (gold).

ments are small over the southern oceans and Oceania, where constraints are weak.

The shift toward earlier springtime emissions in the Northern Hemisphere is one robust feature across our inversions. Thompson et al. (2014c) arrived at the same finding and argued that it reflects the dependence of $N_2O$ emissions on soil moisture and temperature, as drier soils later in summer may limit $N_2O$ fluxes. However, other factors are also likely to contribute. Emissions associated with freeze–thaw cycles can lead to elevated springtime $N_2O$ fluxes at these middle to high latitudes (e.g., Wagner-Riddle et al., 2017), while higher springtime emissions are also consistent with the timing of fertilizer application and indirect $N_2O$ emissions due to leaching and runoff when streamflow is at its peak (Chen et al., 2016; Griffis et al., 2017). The separate spring and summer emission peaks seen over North America in 2011 may reflect the respective influences of indirect and direct emissions, which have been shown (Chen et al., 2016) to peak earlier (indirect emissions) and later (direct emissions) in the growing season. Fall fertilizer application is also common in the US Corn Belt – more than one-third of corn farmers in Minnesota do their main N application during this time (Beirman et al., 2012) – which could explain the October peak in the SVD-based results and provide a source of nitrogen that would be released in the early spring thaw and subsequent runoff period.

We see in Fig. 7 that the seasonal adjustments are larger in the continental and SVD-based inversion than the standard 4D-Var, particularly in regions where direct observational constraints are low. In our previous work (Wells et al., 2015) we highlighted the difficulty in correcting seasonal biases when solving for monthly $N_2O$ emissions on a grid box scale. The SVD-based approach thus provides a major advantage in this context by reducing the dimensions of the inverse problem and allowing us to better resolve temporal features that inform our understanding of $N_2O$ emission processes.

## 5 Conclusions and implications for the $N_2O$ budget

In this paper we employed three inversion frameworks to derive top-down constraints on global monthly $N_2O$ emissions for 2011. The inverse frameworks included (1) a standard 4D-Var inversion at $4° \times 5°$, (2) a 4D-Var inversion solving for fluxes on six continental and three ocean regions, and (3) a fast 4D-Var inversion based on a new dimension reduction technique using efficient randomized-SVD algorithms. The latter technique is an advance over typical aggregation schemes: it defines the optimal resolution of the solution according to the information afforded by the observations, maximizes the DOFs of the inverse system, and offers major time savings compared to other iterative inversion methods.

Over many regions, our inversion results are broadly consistent with other recent inversion studies, though the range of derived flux values and seasonalities from poorly observed regions highlights the ill-posed nature of the inverse problem for $N_2O$. Based on the most robust features across our three different inversion frameworks, we can draw the following conclusions about the global $N_2O$ budget and underlying emission processes:

- The global annual $N_2O$ flux is likely somewhat high in the bottom-up inventory used here, as the lower value ($15.9\,\mathrm{Tg\,N\,yr^{-1}}$) derived in the SVD-based inversion gives a better representation of the $N_2O$ background in the extratropics while also being more consistent with the current best estimate from a 0-D consideration of the global burden and lifetime of $N_2O$ (Prather et al., 2012).

- Our inversion results indicate that a greater fraction of the global $N_2O$ flux is emitted from the tropics than the a priori inventories would suggest. This points to an overestimate of natural soil (and perhaps industrial/residential) emissions in the Northern Hemisphere and to an underestimate of agricultural (and likely oceanic) emissions in the tropics. The former hypothesis would be consistent with the 2-fold reduction in the industrial $N_2O$ source for EDGAR versions subsequent to that used here.

- In the northern hemispheric midlatitudes, $N_2O$ emissions peak in the springtime (March–April). This seasonality is supported by other recent studies and corresponds to the period of higher soil moisture, peak streamflow, thawing of frozen soils, and the timing of fertilizer application.

- We find that $N_2O$ emissions from agricultural soils are underestimated in the US Corn Belt and likely also in Asia. We attribute this to an underestimate of indirect agricultural emissions due to leaching and runoff, freeze–thaw emissions in early spring, and the direct on-field source when N inputs exceed crop demands. Annual emissions over the US Corn Belt are underestimated by 2–3$\times$ in the a priori inventories; the standard and SVD-based inversions used here both increase emissions from this region throughout the growing period (March–September).

Based on our analysis of alternate initial conditions for atmospheric $N_2O$, and their corresponding effects on derived fluxes, we recommend formally optimizing the initial mass field (either alone or in tandem with the emissions optimization) rather than interpolating $N_2O$ observations or using an unconstrained model spinup. The impacts can be substantial: for the sensitivity tests used here, a posteriori global fluxes ranged by $\sim 25\,\%$ ($16.1$–$21.4\,\mathrm{Tg\,N\,yr^{-1}}$) across different treatments of the initial $N_2O$ mass.

Finally, the SVD-based inverse approach used here offers a powerful framework for maximizing the emission information derived from atmospheric observations of $N_2O$

in an efficient, timely manner, particularly for models with a low level of parallelization. The approach provides valuable spatially resolved information that is lost when solving for fluxes over ad hoc continental-scale regions, while also providing a much stronger ability to resolve broad temporal features than is possible with a standard 4D-Var inversion at the model grid resolution. Such information is key to furthering our understanding of $N_2O$ emission processes based on top-down analyses.

*Code availability.* The $N_2O$ version of the GEOS-Chem adjoint code is available via the GEOS-Chem adjoint repository. Instructions for obtaining access to the code can be found at http://wiki.seas.harvard.edu/geos-chem/index.php/GEOS-Chem_Adjoint.

*Data availability.* $N_2O$ measurements used in this work are available from NOAA ESRL/GMD (http://www.esrl.noaa.gov/gmd/dv/data/) and the World Data Centre for Greenhouse Gases (http://ds.data.jma.go.jp/gmd/wdcgg/) or by contacting the principle investigators of the individual measurement stations.

## Appendix A: Proof for cost function projection formula

$$J(\boldsymbol{x}) = \frac{1}{2}(\boldsymbol{h}(\boldsymbol{x}) - \boldsymbol{y})^T \mathbf{S}_y^{-1} (\boldsymbol{h}(\boldsymbol{x}) - \boldsymbol{y}) + \frac{1}{2}(\boldsymbol{x} - \boldsymbol{x}_a)^T \mathbf{S}_a^{-1} (\boldsymbol{x} - \boldsymbol{x}_a), \tag{A1}$$

and

$$\boldsymbol{h}(\boldsymbol{x}) = \boldsymbol{h}(\boldsymbol{x}_a) + \mathbf{H}(\boldsymbol{x} - \boldsymbol{x}_a). \tag{A2}$$

Therefore,

$$\begin{aligned}
&(\boldsymbol{h}(\boldsymbol{x}) - \boldsymbol{y})^T \mathbf{S}_y^{-1} (\boldsymbol{h}(\boldsymbol{x}) - \boldsymbol{y}) = \\
&(\boldsymbol{h}(\boldsymbol{x}_a) + \mathbf{H}(\boldsymbol{x} - \boldsymbol{x}_a) - \boldsymbol{y})^T \mathbf{S}_y^{-1} (\boldsymbol{h}(\boldsymbol{x}_a) + \mathbf{H}(\boldsymbol{x} - \boldsymbol{x}_a) - \boldsymbol{y}) = \\
&\left(\boldsymbol{h}(\boldsymbol{x}_a) + \mathbf{S}_y^{\frac{1}{2}} \mathbf{S}_y^{-\frac{1}{2}} \mathbf{H} \mathbf{S}_a^{\frac{1}{2}} \mathbf{S}_a^{-\frac{1}{2}} (\boldsymbol{x} - \boldsymbol{x}_a) - \boldsymbol{y}\right)^T \\
&\times \mathbf{S}_y^{-1} \left(\boldsymbol{h}(\boldsymbol{x}_a) + \mathbf{S}_y^{\frac{1}{2}} \mathbf{S}_y^{-\frac{1}{2}} \mathbf{H} \mathbf{S}_a^{\frac{1}{2}} \mathbf{S}_a^{-\frac{1}{2}} (\boldsymbol{x} - \boldsymbol{x}_a) - \boldsymbol{y}\right).
\end{aligned} \tag{A3}$$

Then we develop $\mathbf{S}_y^{-\frac{1}{2}} \mathbf{H} \mathbf{S}_a^{\frac{1}{2}} = \sum_{i=1}^{n} \lambda_i^{\frac{1}{2}} \boldsymbol{w}_i \boldsymbol{v}_i^T$, where $n$ is the dimension of the state vector, and project the control variable onto the optimal basis $\{\boldsymbol{S}_a^{\frac{1}{2}} \boldsymbol{v}_i, i = 1, \ldots, k\}$ using the projector $\pi = \mathbf{S}_a^{\frac{1}{2}} \sum_{i=1}^{k} \boldsymbol{v}_i \boldsymbol{v}_i^T \mathbf{S}_a^{-\frac{1}{2}}$, which yields

$$\begin{aligned}
&(\boldsymbol{h}(\boldsymbol{x}) - \boldsymbol{y})^T \mathbf{S}_y^{-1} (\boldsymbol{h}(\boldsymbol{x}) - \boldsymbol{y}) \approx \\
&(\boldsymbol{h}(\boldsymbol{x}_a) - \boldsymbol{y})^T \mathbf{S}_y^{-1} (\boldsymbol{h}(\boldsymbol{x}_a) - \boldsymbol{y}) \\
&+ (\boldsymbol{x} - \boldsymbol{x}_a)^T \mathbf{S}_a^{-\frac{1}{2}} \sum_{i=1}^{k} \lambda_i \boldsymbol{v}_i \boldsymbol{v}_i^T \mathbf{S}_a^{-\frac{1}{2}} (\boldsymbol{x} - \boldsymbol{x}_a) \\
&+ (\boldsymbol{h}(\boldsymbol{x}_a) - \boldsymbol{y})^T \mathbf{S}_y^{-\frac{1}{2}} \sum_{i=1}^{k} \lambda_i^{\frac{1}{2}} \boldsymbol{w}_i \boldsymbol{v}_i^T \mathbf{S}_a^{-\frac{1}{2}} (\boldsymbol{x} - \boldsymbol{x}_a) \\
&+ (\boldsymbol{x} - \boldsymbol{x}_a)^T \mathbf{S}_a^{-\frac{1}{2}} \sum_{i=1}^{k} \lambda_i^{\frac{1}{2}} \boldsymbol{v}_i \boldsymbol{w}_i^T \mathbf{S}_y^{-\frac{1}{2}} (\boldsymbol{h}(\boldsymbol{x}_a) - \boldsymbol{y}),
\end{aligned} \tag{A4}$$

and

$$\begin{aligned}
&(\boldsymbol{x} - \boldsymbol{x}_a)^T \mathbf{S}_a^{-1} (\boldsymbol{x} - \boldsymbol{x}_a) \approx \\
&(\boldsymbol{x} - \boldsymbol{x}_a)^T \mathbf{S}_a^{-\frac{1}{2}} \sum_{i=1}^{k} \boldsymbol{v}_i \boldsymbol{v}_i^T \mathbf{S}_a^{-\frac{1}{2}} (\boldsymbol{x} - \boldsymbol{x}_a).
\end{aligned} \tag{A5}$$

Inserting Eqs. (A4) and (A5) in Eq. (A1), one obtains

$$\begin{aligned}
J(\boldsymbol{x}) \approx &\frac{1}{2}(\boldsymbol{x} - \boldsymbol{x}_a)^T \mathbf{S}_a^{-\frac{1}{2}} \sum_{i=1}^{k} \boldsymbol{v}_i \boldsymbol{v}_i^T \mathbf{S}_a^{-\frac{1}{2}} (\boldsymbol{x} - \boldsymbol{x}_a) \\
&+ \frac{1}{2}(\boldsymbol{h}(\boldsymbol{x}_a) - \boldsymbol{y})^T \mathbf{S}_y^{-1} (\boldsymbol{h}(\boldsymbol{x}_a) - \boldsymbol{y}) \\
&+ \frac{1}{2}(\boldsymbol{x} - \boldsymbol{x}_a)^T \mathbf{S}_a^{-\frac{1}{2}} \sum_{i=1}^{k} \lambda_i \boldsymbol{v}_i \boldsymbol{v}_i^T \mathbf{S}_a^{-\frac{1}{2}} (\boldsymbol{x} - \boldsymbol{x}_a) \\
&+ \frac{1}{2}(\boldsymbol{h}(\boldsymbol{x}_a) - \boldsymbol{y})^T \mathbf{S}_y^{-\frac{1}{2}} \sum_{i=1}^{k} \lambda_i^{\frac{1}{2}} \boldsymbol{w}_i \boldsymbol{v}_i^T \mathbf{S}_a^{-\frac{1}{2}} (\boldsymbol{x} - \boldsymbol{x}_a) \\
&+ \frac{1}{2}(\boldsymbol{x} - \boldsymbol{x}_a)^T \mathbf{S}_a^{-\frac{1}{2}} \sum_{i=1}^{k} \lambda_i^{\frac{1}{2}} \boldsymbol{v}_i \boldsymbol{w}_i^T \mathbf{S}_y^{-\frac{1}{2}} (\boldsymbol{h}(\boldsymbol{x}_a) - \boldsymbol{y}).
\end{aligned} \tag{A6}$$

Differentiating Eq. (A6), one obtains

$$\begin{aligned}
\nabla J(\boldsymbol{x}) \approx &\mathbf{S}_a^{-\frac{1}{2}} \sum_{i=1}^{k} \boldsymbol{v}_i \boldsymbol{v}_i^T \mathbf{S}_a^{-\frac{1}{2}} (\boldsymbol{x} - \boldsymbol{x}_a) \\
&+ \mathbf{S}_a^{-\frac{1}{2}} \sum_{i=1}^{k} \lambda_i \boldsymbol{v}_i \boldsymbol{v}_i^T \mathbf{S}_a^{-\frac{1}{2}} (\boldsymbol{x} - \boldsymbol{x}_a) \\
&+ \mathbf{S}_a^{-\frac{1}{2}} \sum_{i=1}^{k} \lambda_i^{\frac{1}{2}} \boldsymbol{v}_i \boldsymbol{w}_i^T \mathbf{S}_y^{-\frac{1}{2}} (\boldsymbol{h}(\boldsymbol{x}_a) - \boldsymbol{y}).
\end{aligned} \tag{A7}$$

**The Supplement related to this article is available online at https://doi.org/10.5194/acp-18-735-2018-supplement.**

*Competing interests.* The authors declare that they have no conflict of interest.

*Acknowledgements.* This work was supported by NOAA (grant no. NA13OAR4310086 and NA13OAR4310081) and the Minnesota Supercomputing Institute. The KCMP measurements were made with support from the USDA (grant no. 2013-67019-21364). We thank E. Kort and S. Wofsy for providing the HIPPO $N_2O$ measurements. We thank Environment Canada for providing data from the Alert, Churchill, Estevan Point, East Trout Lake, Fraserdale, and Sable Island Sites. We thank R. Martin and S. Nichol for providing data from the Arrival Heights NIWA station. We thank J. Muhle and C. Harth (UCSD-SIO), P. Fraser (CSIRO), R. Wang (GaTech), and other members of the AGAGE team for providing AGAGE data. The AGAGE Mace Head, Trinidad Head, Cape Matatula, Ragged Point, and Cape Grim stations are supported by NASA grants to the Massachusetts Institute of Technology and Scripps Institution of Oceanography, the Department of Energy and Climate Change (DECC, UK) contract to the University of Bristol, and CSIRO and the Australian Bureau of Meteorology. We thank C. Adam Schlosser for work on the MIT IGSM.

Edited by: Annmarie Carlton
Reviewed by: two anonymous referees

## References

Beaulieu, J. J., Tank, J. L., Hamilton, S. K., Wollheim, W. M., Hall, R. O., Mulholland, P. J., Peterson, B. J., Ashkenas, L. R., Cooper, L. W., Dahm, C. N., Dodds, W. K., Grimm, N. B., Johnson, S. L., McDowell, W. H., Poole, G. C., Valett, H. M., Arango, C. P., Bernot, M. J., Burgin, A. J., Crenshaw, C. L., Helton, A. M., Johnson, L. T., O'Brien, J. M., Potter, J. D., Sheibley, R. W., Sobota, D. J., and Thomas, S. M.: Nitrous oxide emission from denitrification in stream and river networks, P. Natl. Acad. Sci. USA, 108, 214–219, https://doi.org/10.1073/pnas.1011464108, 2011.

Beirman, P., Rosen, C., Venterea, R., and Lamb, J.: Survey of nitrogen fertilizer use on corn in Minnesota, Agr. Syst., 109, 43–52, 2012.

Bocquet, M., Wu, L., and Chevallier, F.: Bayesian design of control space for optimal assimilation of observations. Part I: Consistent multiscale formalism, Q. J. Roy. Meteor. Soc., 137, 1340–1356, https://doi.org/10.1002/qj.837, 2011.

Bousserez, N. and Henze, D. K.: Optimal and scalable methods to approximate the solutions of large-scale Bayesian problems: theory and application to atmospheric inversions and data assimilation, accepted, https://doi.org/10.1002/qj.3209, 2017.

Bouwman, A. F.: Environmental science – nitrogen oxides and tropical agriculture, Nature, 392, 866–867, https://doi.org/10.1038/31809, 1998.

Bouwman, A. F., Beusen, A. H. W., Griffioen, J., Van Groenigen, J. W., Hefting, M. M., Oenema, O., Van Puijenbroek, P. J. T. M., Seitzinger, S., Slomp, C. P., and Stehfest, E.: Global trends and uncertainties in terrestrial denitrification and $N_2O$ emissions, Philos. T. R. Soc. B, 368, 20130112, https://doi.org/10.1098/rstb.2013.0112, 2013.

Bui-Thanh, T., Burstedde, C., Ghattas, O., Martin, J., Stadler, G., and Wilcox, L. C.: Extreme-Scale UQ for Bayesian Inverse Problems Governed by PDEs, in: International Conference for High Performance Computing Networking Storage and Analysis, 25th ACM/IEEE International Conference for High Performance Computing, Networking, Storage and Analysis (SC), Salt Lake City, UT, 2012, WOS:000316911000003, 2012.

Buitenhuis, E. T., Suntharalingam, P., and Le Quéré, C.: Constraints on global oceanic emissions of $N_2O$ from observations and models, Biogeosciences Discuss., https://doi.org/10.5194/bg-2017-193, in review, 2017.

Butterbach-Bahl, K., Baggs, E. M., Dannenmann, M., Kiese, R., and Zechmeister-Boltenstern, S.: Nitrous oxide emissions from soils: how well do we understand the processes and their controls?, Philos. T. R. Soc. B, 368, 20140122, https://doi.org/10.1098/rstb.2013.0122, 2013.

Byrd, R. H., Lu, P. H., Nocedal, J., and Zhu, C. Y.: A limited memory algorithm for bound constrained optimization, SIAM J. Sci. Comput., 16, 1190–1208, https://doi.org/10.1137/0916069, 1995.

Chen, Z. C., Griffis, T. J., Millet, D. B., Wood, J. D., Lee, X., Baker, J. M., Xiao, K., Turner, P. A., Chen, M., Zobitz, J., and Wells, K. C.: Partitioning $N_2O$ emissions within the US Corn Belt using an inverse modeling approach, Global Biogeochem. Cy., 30, 1192–1205, https://doi.org/10.1002/2015gb005313, 2016.

Cohen, Y. and Gordon, L. I.: Nitrous oxide production in the ocean, J. Geophys. Res.-Oc. Atm., 84, 347–353, https://doi.org/10.1029/JC084iC01p00347, 1979.

Corazza, M., Bergamaschi, P., Vermeulen, A. T., Aalto, T., Haszpra, L., Meinhardt, F., O'Doherty, S., Thompson, R., Moncrieff, J., Popa, E., Steinbacher, M., Jordan, A., Dlugokencky, E., Brühl, C., Krol, M., and Dentener, F.: Inverse modelling of European $N_2O$ emissions: assimilating observations from different networks, Atmos. Chem. Phys., 11, 2381–2398, https://doi.org/10.5194/acp-11-2381-2011, 2011.

Crutzen, P. J., Mosier, A. R., Smith, K. A., and Winiwarter, W.: $N_2O$ release from agro-biofuel production negates global warming reduction by replacing fossil fuels, Atmos. Chem. Phys., 8, 389–395, https://doi.org/10.5194/acp-8-389-2008, 2008.

Cui, T., Martin, J., Marzouk, Y. M., Solonen, A., and Spantini, A.: Likelihood-informed dimension reduction for nonlinear inverse problems, Inverse Probl., 30, 114015, https://doi.org/10.1088/0266-5611/30/11/114015, 2014.

Davidson, E. A.: The contribution of manure and fertilizer nitrogen to atmospheric nitrous oxide since 1860, Nat. Geosci., 2, 659–662, https://doi.org/10.1038/ngeo608, 2009.

Deng, F., Jones, D. B. A., Henze, D. K., Bousserez, N., Bowman, K. W., Fisher, J. B., Nassar, R., O'Dell, C., Wunch, D., Wennberg, P. O., Kort, E. A., Wofsy, S. C., Blumenstock, T., Deutscher, N. M., Griffith, D. W. T., Hase, F., Heikkinen, P., Sherlock, V., Strong, K., Sussmann, R., and Warneke, T.: Inferring regional sources and sinks of atmospheric $CO_2$ from GOSAT $XCO_2$ data, At-

mos. Chem. Phys., 14, 3703–3727, https://doi.org/10.5194/acp-14-3703-2014, 2014.

Deng, F., Jones, D. B. A., Walker, T. W., Keller, M., Bowman, K. W., Henze, D. K., Nassar, R., Kort, E. A., Wofsy, S. C., Walker, K. A., Bourassa, A. E., and Degenstein, D. A.: Sensitivity analysis of the potential impact of discrepancies in stratosphere–troposphere exchange on inferred sources and sinks of $CO_2$, Atmos. Chem. Phys., 15, 11773–11788, https://doi.org/10.5194/acp-15-11773-2015, 2015.

Dlugokencky, E. J., Steele, L. P., Lang, P. M., and Masarie, K. A.: The growth rate and distribution of atmospheric methane, J. Geophys. Res.-Atmos., 99, 17021–17043, https://doi.org/10.1029/94jd01245, 1994.

Elkins, J. W., Wofsy, S. C., McElroy, M. B., Kolb, C. E., and Kaplan, W. A.: Aquatic sources and sinks for nitrous oxide, Nature, 275, 602–606, https://doi.org/10.1038/275602a0, 1978.

Firestone, M. K. and Davidson, E. A.: Microbiological basis of NO and $N_2O$ production and consumption in the soil, in: Exchange of Trace Gases Between Terrestrial Ecosystems and the Atmosphere, edited by: Andreae, M. O., and Schimel, D. S., Wiley and Sons, Chichester, 7–21, 1989.

Flath, H. P., Wilcox, L. C., Akcelik, V., Hill, J., Waanders, B. V., and Ghattas, O.: Fast algorithms for Bayesian uncertainty quantification in large-scale linear inverse problems based on low-rank partial Hessian approximations, SIAM J. Sci. Comput., 33, 407–432, https://doi.org/10.1137/090780717, 2011.

Galloway, J. N., Townsend, A. R., Erisman, J. W., Bekunda, M., Cai, Z. C., Freney, J. R., Martinelli, L. A., Seitzinger, S. P., and Sutton, M. A.: Transformation of the nitrogen cycle: Recent trends, questions, and potential solutions, Science, 320, 889–892, https://doi.org/10.1126/science.1136674, 2008.

Gerber, J. S., Carlson, K. M., Makowski, D., Mueller, N. D., Garcia de Cortazar-Atauri, I., Havlík, P., Herrero, M., Launay, M., O'Connell, C. S., Smith, P., and West, P. C.: Spatially explicit estimates of $N_2O$ emissions from croplands suggest climate mitigation opportunities from improved fertilizer management, Glob. Change Biol., 22, 3383–3394, https://doi.org/10.1111/gcb.13341, 2016.

Griffis, T. J., Lee, X., Baker, J. M., Russelle, M. P., Zhang, X., Venterea, R., and Millet, D. B.: Reconciling the differences between top-down and bottom-up estimates of nitrous oxide emissions for the US Corn Belt, Global Biogeochem. Cy., 27, 746–754, https://doi.org/10.1002/gbc.20066, 2013.

Griffis, T. J., Chen, Z., Baker, J. M., Wood, J. D., Millet, D. B., Lee, X., Venterea, R. T., and Turner, P. A.: Nitrous oxide emissions are enhanced in a warmer and wetter world, P. Natl. Acad. Sci. USA, 114, 12081–12085, https://doi.org/10.1073/pnas.1704552114, 2017.

Hall, B. D., Dutton, G. S., and Elkins, J. W.: The NOAA nitrous oxide standard scale for atmospheric observations, J. Geophys. Res., 112, D09305, https://doi.org/10.1029/2006JD007954, 2007.

Halko, N., Martinsson, P. G., and Tropp, J. A.: Finding structure with randomness: Probabilistic algorithms for constructing approximate matrix decompositions, SIAM Rev., 53, 217–288, https://doi.org/10.1137/090771806, 2011.

Henze, D. K., Hakami, A., and Seinfeld, J. H.: Development of the adjoint of GEOS-Chem, Atmos. Chem. Phys., 7, 2413–2433, https://doi.org/10.5194/acp-7-2413-2007, 2007.

Hirsch, A. I., Michalak, A. M., Bruhwiler, L. M., Peters, W., Dlugokencky, E. J., and Tans, P. P.: Inverse modeling estimates of the global nitrous oxide surface flux from 1998–2001, Global Biogeochem. Cy., 20, GB1008, https://doi.org/10.1029/2004gb002443, 2006.

Huang, J., Golombek, A., Prinn, R., Weiss, R., Fraser, P., Simmonds, P., Dlugokencky, E. J., Hall, B., Elkins, J., Steele, P., Langenfelds, R., Krummel, P., Dutton, G., and Porter, L.: Estimation of regional emissions of nitrous oxide from 1997 to 2005 using multinetwork measurements, a chemical transport model, and an inverse method, J. Geophys. Res., 113, D17313, https://doi.org/10.1029/2007jd009381, 2008.

International Fertilizer Association: IFA, available at: http://www.fertilizer.org/statistics, last accessed: 15 June 2016.

Jin, X. and Gruber, N.: Offsetting the radiative benefit of ocean iron fertilization by enhancing $N_2O$ emissions, Geophys. Res. Lett., 30, 2249, https://doi.org/10.1029/2003gl018458, 2003.

Kaminski, T. and Heimann, M.: Inverse modeling of atmospheric carbon dioxide fluxes, Science, 294, U1–U1, 2001.

Kopacz, M., Jacob, D. J., Henze, D. K., Heald, C. L., Streets, D. G., and Zhang, Q.: Comparison of adjoint and analytical Bayesian inversion methods for constraining Asian sources of carbon monoxide using satellite (MOPITT) measurements of CO columns, J. Geophys. Res.-Atmos., 114, D04305, https://doi.org/10.1029/2007jd009264, 2009.

Kim, D.-G., Vargas, R., Bond-Lamberty, B., and Turetsky, M. R.: Effects of soil rewetting and thawing on soil gas fluxes: a review of current literature and suggestions for future research, Biogeosciences, 9, 2459–2483, https://doi.org/10.5194/bg-9-2459-2012, 2012.

Kort, E. A., Eluszkiewicz, J., Stephens, B. B., Miller, J. B., Gerbig, C., Nehrkorn, T., Daube, B. C., Kaplan, J. O., Houweling, S., and Wofsy, S. C.: Emissions of $CH_4$ and $N_2O$ over the United States and Canada based on a receptor-oriented modeling framework and COBRA-NA atmospheric observations, Geophys. Res. Lett., 35, L18808, https://doi.org/10.1029/2008gl034031, 2008.

Kort, E. A., Patra, P. K., Ishijima, K., Daube, B. C., Jimenez, R., Elkins, J., Hurst, D., Moore, F. L., Sweeney, C., and Wofsy, S. C.: Tropospheric distribution and variability of $N_2O$: Evidence for strong tropical emissions, Geophys. Res. Lett., 38, L15806, https://doi.org/10.1029/2011gl047612, 2011.

Lambert, A., Read, W. G., Livesey, N. J., Santee, M. L., Manney, G. L., Froidevaux, L., Wu, D. L., Schwartz, M. J., Pumphrey, H. C., Jimenez, C., Nedoluha, G. E., Cofield, R. E., Cuddy, D. T., Daffer, W. H., Drouin, B. J., Fuller, R. A., Jarnot, R. F., Knosp, B. W., Pickett, H. M., Perun, V. S., Snyder, W. V., Stek, P. C., Thurstans, R. P., Wagner, P. A., Waters, J. W., Jucks, K. W., Toon, G. C., Stachnik, R. A., Bernath, P. F., Boone, C. D., Walker, K. A., Urban, J., Murtagh, D., Elkins, J. W., and Atlas, E.: Validation of the Aura Microwave Limb Sounder middle atmosphere water vapor and nitrous oxide measurements, J. Geophys. Res.-Atmos., 112, D24S26, https://doi.org/10.1029/2007jd008724, 2007.

Liu, J. J., Bowman, K. W., Lee, M., Henze, D. K., Bousserez, N., Brix, H., Collatz, G. J., Menemenlis, D., Ott, L., Pawson, S., Jones, D., and Nassar, R.: Carbon monitoring system flux estimation and attribution: impact of ACOS-GOSAT X-$CO_2$ sampling on the inference of terrestrial biospheric sources and sinks, Tellus B, 66, 22486, https://doi.org/10.3402/tellusb.v66.22486, 2014.

Liu, J. J., Bowman, K. W., and Henze, D. K.: Source-receptor relationships of column-average $CO_2$ and implications for the impact of observations on flux inversions, J. Geophys. Res., 120, 5214–5236, https://doi.org/10.1002/2014jd022914, 2015.

Manizza, M., Keeling, R. F., and Nevison, C. D.: On the processes controlling the seasonal cycles of the air–sea fluxes of $O_2$ and $N_2O$: a modelling study, Tellus B, 64, 18429, https://doi.org/10.3402/tellusb.v64i0.18429, 2012.

Miller, S. M., Kort, E. A., Hirsch, A. I., Dlugokencky, E. J., Andrews, A. E., Xu, X., Tian, H., Nehrkorn, T., Eluszkiewicz, J., Michalak, A. M., and Wofsy, S. C.: Regional sources of nitrous oxide over the United States: Seasonal variation and spatial distribution, J. Geophys. Res., 117, D06310, https://doi.org/10.1029/2011jd016951, 2012.

Mosier, A., Kroeze, C., Nevison, C., Oenema, O., Seitzinger, S., and van Cleemput, O.: Closing the global $N_2O$ budget: nitrous oxide emissions through the agricultural nitrogen cycle - OECD/IPCC/IEA phase II development of IPCC guidelines for national greenhouse gas inventory methodology, Nutr. Cycl. Agroecosys., 52, 225–248, https://doi.org/10.1023/a:1009740530221, 1998.

Myhre, G., Shindell, D., Bréon, F.-M., Collins, W., Fuglestvedt, J., Huang, J., Koch, D., Lamarque, J.-F., Lee, D., Mendoza, B., Nakajima, T., Robock, A., Stephens, G., Takemura, T., and Zhang, H.: Anthropogenic and natural radiative forcing, in: Climate Change 2013: The Physical Science Basis. Contribution of Working Group I to the Fifth Assessment Report of the Intergovernmental Panel on Climate Change, edited by: Stocker, T. F., Qin, D., Plattner, G.-K., Tignor, M., Allen, S. K., Boschung, J., Nauels, A., Xia, Y., Bex, V., Midgley, P. M., Cambridge, UK, and New York, NY, USA, 2013.

Nevison, C. D., Weiss, R. F., and Erickson, D. J.: Global oceanic emissions of nitrous oxide, J. Geophys. Res.-Oceans, 100, 15809–15820, https://doi.org/10.1029/95jc00684, 1995.

NOAA ESRL/GMD: http://www.esrl.noaa.gov/gmd/dv/data/, 2017.

Park, S., Croteau, P., Boering, K. A., Etheridge, D. M., Ferretti, D., Fraser, P. J., Kim, K. R., Krummel, P. B., Langenfelds, R. L., van Ommen, T. D., Steele, L. P., and Trudinger, C. M.: Trends and seasonal cycles in the isotopic composition of nitrous oxide since 1940, Nat. Geosci., 5, 261–265, https://doi.org/10.1038/ngeo1421, 2012.

Potter, C. S., Matson, P. A., Vitousek, P. M., and Davidson, E. A.: Process modeling of controls on nitrogen trace gas emissions from soils worldwide, J. Geophys. Res.-Atmos., 101, 1361–1377, https://doi.org/10.1029/95jd02028, 1996.

Prather, M., Ehhalt, D., Dentener, F., Derwent, R., Dlugokencky, E., Holland, E., Isaksen, I., Katima, J., Kirchhoff, V., Matson, P., Midgley, P., and Wang, M.: Atmospheric chemistry and greenhouse gases, in Climate Change 2011: The Scientific Basis. Third Annual Assessment Report of the Intergovernmental Panel on Climate Change, edited by: Joos, F., and McFarland, M., Cambridge University Press, Cambridge, UK, 239–287, 2001.

Prather, M. J., Holmes, C. D., and Hsu, J.: Reactive greenhouse gas scenarios: Systematic exploration of uncertainties and the role of atmospheric chemistry, Geophys. Res. Lett., 39, L09803, https://doi.org/10.1029/2012gl051440, 2012.

Prinn, R. G., Weiss, R. F., Fraser, P. J., Simmonds, P. G., Cunnold, D. M., Alyea, F. N., O'Doherty, S., Salameh, P., Miller, B. R., Huang, J., Wang, R. H. J., Hartley, D. E., Harth, C., Steele, L. P., Sturrock, G., Midgley, P. M., and McCulloch, A.: A history of chemically and radiatively important gases in air deduced from ALE/GAGE/AGAGE, J. Geophys. Res., 105, 17751–17792, https://doi.org/10.1029/2000jd900141, 2000.

Ravishankara, A. R., Daniel, J. S., and Portmann, R. W.: Nitrous Oxide ($N_2O$): The Dominant Ozone-Depleting Substance Emitted in the 21st Century, Science, 326, 123–125, https://doi.org/10.1126/science.1176985, 2009.

Saikawa, E., Schlosser, C. A., and Prinn, R. G.: Global modeling of soil nitrous oxide emissions from natural processes, Global Biogeochem. Cy., 27, 972–989, https://doi.org/10.1002/gbc.20087, 2013.

Saikawa, E., Prinn, R. G., Dlugokencky, E., Ishijima, K., Dutton, G. S., Hall, B. D., Langenfelds, R., Tohjima, Y., Machida, T., Manizza, M., Rigby, M., O'Doherty, S., Patra, P. K., Harth, C. M., Weiss, R. F., Krummel, P. B., van der Schoot, M., Fraser, P. J., Steele, L. P., Aoki, S., Nakazawa, T., and Elkins, J. W.: Global and regional emissions estimates for $N_2O$, Atmos. Chem. Phys., 14, 4617–4641, https://doi.org/10.5194/acp-14-4617-2014, 2014.

Seitzinger, S. P. and Kroeze, C.: Global distribution of nitrous oxide production and N inputs in freshwater and coastal marine ecosystems, Global Biogeochem. Cy., 12, 93–113, https://doi.org/10.1029/97gb03657, 1998.

Shcherbak, I., Millar, N., and Robertson, G. P.: Global metaanalysis of the nonlinear response of soil nitrous oxide ($N_2O$) emissions to fertilizer nitrogen, P. Natl. Acad. Sci. USA, 111, 9199–9204, https://doi.org/10.1073/pnas.1322434111, 2014.

Sokolov, A. P., Stone, P. H., Forest, C. E., Prinn, R., Sarofim, M. C., Webster, M., Saltsev, S., and Schlosser, C. A.: Probabilistic forecast for twenty-first-century climate based on uncertainties in emissions (without policy) and climate parameters, J. Climate, 5175–5204, https://doi.org/10.1175/2009JCLI2863.1, 2009.

Spantini, A., Solonen, A., Cui, T. G., Martin, J., Tenorio, L., and Marzouk, Y.: Optimal low-rank approximations of Bayesian linear inverse problems, SIAM J. Sci. Comput., 37, A2451–A2487, https://doi.org/10.1137/140977308, 2015.

Thompson, R. L., Bousquet, P., Chevallier, F., Rayner, P. J., and Ciais, P.: Impact of the atmospheric sink and vertical mixing on nitrous oxide fluxes estimated using inversion methods, J. Geophys. Res., 116, D17307, https://doi.org/10.1029/2011jd015815, 2011.

Thompson, R. L., Chevallier, F., Crotwell, A. M., Dutton, G., Langenfelds, R. L., Prinn, R. G., Weiss, R. F., Tohjima, Y., Nakazawa, T., Krummel, P. B., Steele, L. P., Fraser, P., O'Doherty, S., Ishijima, K., and Aoki, S.: Nitrous oxide emissions 1999 to 2009 from a global atmospheric inversion, Atmos. Chem. Phys., 14, 1801–1817, https://doi.org/10.5194/acp-14-1801-2014, 2014a.

Thompson, R. L., Patra, P. K., Ishijima, K., Saikawa, E., Corazza, M., Karstens, U., Wilson, C., Bergamaschi, P., Dlugokencky, E., Sweeney, C., Prinn, R. G., Weiss, R. F., O'Doherty, S., Fraser, P. J., Steele, L. P., Krummel, P. B., Saunois, M., Chipperfield, M., and Bousquet, P.: TransCom $N_2O$ model inter-comparison – Part 1: Assessing the influence of transport and surface fluxes on tropospheric $N_2O$ variability, Atmos. Chem. Phys., 14, 4349–4368, https://doi.org/10.5194/acp-14-4349-2014, 2014b.

Thompson, R. L., Ishijima, K., Saikawa, E., Corazza, M., Karstens, U., Patra, P. K., Bergamaschi, P., Chevallier, F., Dlugokencky,

E., Prinn, R. G., Weiss, R. F., O'Doherty, S., Fraser, P. J., Steele, L. P., Krummel, P. B., Vermeulen, A., Tohjima, Y., Jordan, A., Haszpra, L., Steinbacher, M., Van der Laan, S., Aalto, T., Meinhardt, F., Popa, M. E., Moncrieff, J., and Bousquet, P.: TransCom $N_2O$ model inter-comparison – Part 2: Atmospheric inversion estimates of $N_2O$ emissions, Atmos. Chem. Phys., 14, 6177–6194, https://doi.org/10.5194/acp-14-6177-2014, 2014c.

Turner, A. J., Jacob, D. J., Wecht, K. J., Maasakkers, J. D., Lundgren, E., Andrews, A. E., Biraud, S. C., Boesch, H., Bowman, K. W., Deutscher, N. M., Dubey, M. K., Griffith, D. W. T., Hase, F., Kuze, A., Notholt, J., Ohyama, H., Parker, R., Payne, V. H., Sussmann, R., Sweeney, C., Velazco, V. A., Warneke, T., Wennberg, P. O., and Wunch, D.: Estimating global and North American methane emissions with high spatial resolution using GOSAT satellite data, Atmos. Chem. Phys., 15, 7049–7069, https://doi.org/10.5194/acp-15-7049-2015, 2015a.

Turner, P. A., Griffis, T. J., Lee, X. H., Baker, J. M., Venterea, R. T., and Wood, J. D.: Indirect nitrous oxide emissions from streams within the US Corn Belt scale with stream order, P. Natl. Acad. Sci. USA, 112, 9839–9843, https://doi.org/10.1073/pnas.1503598112, 2015b.

van der Werf, G. R., Randerson, J. T., Giglio, L., Collatz, G. J., Mu, M., Kasibhatla, P. S., Morton, D. C., DeFries, R. S., Jin, Y., and van Leeuwen, T. T.: Global fire emissions and the contribution of deforestation, savanna, forest, agricultural, and peat fires (1997–2009), Atmos. Chem. Phys., 10, 11707–11735, https://doi.org/10.5194/acp-10-11707-2010, 2010.

Volk, C. M., Elkins, J. W., Fahey, D. W., Dutton, G. S., Gilligan, J. M., Loewenstein, M., Podolske, J. R., Chan, K. R., and Gunson, M. R.: Evaluation of source gas lifetimes from stratospheric observations, J. Geophys. Res.-Atmos., 102, 25543–25564, https://doi.org/10.1029/97jd02215, 1997.

Wagner-Riddle, C., Congreves, K. A., Abalos, D., Berg, A. A., Brown, S. E., Ambadan, J. T., Gao, X. P., and Tenuta, M.: Globally important nitrous oxide emissions from croplands induced by freeze–thaw cycles, Nat. Geosci., 10, 279–283, https://doi.org/10.1038/ngeo2907, 2017.

Wecht, K. J., Jacob, D. J., Sulprizio, M. P., Santoni, G. W., Wofsy, S. C., Parker, R., Bösch, H., and Worden, J.: Spatially resolving methane emissions in California: constraints from the CalNex aircraft campaign and from present (GOSAT, TES) and future (TROPOMI, geostationary) satellite observations, Atmos. Chem. Phys., 14, 8173–8184, https://doi.org/10.5194/acp-14-8173-2014, 2014.

Wells, K. C., Millet, D. B., Cady-Pereira, K. E., Shephard, M. W., Henze, D. K., Bousserez, N., Apel, E. C., de Gouw, J., Warneke, C., and Singh, H. B.: Quantifying global terrestrial methanol emissions using observations from the TES satellite sensor, Atmos. Chem. Phys., 14, 2555–2570, https://doi.org/10.5194/acp-14-2555-2014, 2014.

Wells, K. C., Millet, D. B., Bousserez, N., Henze, D. K., Chaliyakunnel, S., Griffis, T. J., Luan, Y., Dlugokencky, E. J., Prinn, R. G., O'Doherty, S., Weiss, R. F., Dutton, G. S., Elkins, J. W., Krummel, P. B., Langenfelds, R., Steele, L. P., Kort, E. A., Wofsy, S. C., and Umezawa, T.: Simulation of atmospheric $N_2O$ with GEOS-Chem and its adjoint: evaluation of observational constraints, Geosci. Model Dev., 8, 3179–3198, https://doi.org/10.5194/gmd-8-3179-2015, 2015.

Wofsy, S. C.: HIAPER Pole-to-Pole Observations (HIPPO): fine-grained, global-scale measurements of climatically important atmospheric gases and aerosols, Philos. T. Roy. Soc. A, 369, 2073–2086, https://doi.org/10.1098/rsta.2010.0313, 2011.

World Data Centre for Greenhouse Gases (WDCGG): http://ds.data.jma.go.jp/gmd/wdcgg/, 2017.

Zhu, C., Byrd, R. H., Lu, P., and Nocedal, J.: L-BFGS-B: a limited memory FORTRAN code for solving bound constrained optimization problems, Tech. rep., Northwestern University, Evanston, Illinois, 1994.